Stony Brook University

Models and Numerical Algorithms for Hydrodynamics with Atomic Processes and High Energy Density Applications

A Dissertation Presented

by

Hyoungkeun Kim

to

The Graduate School

in Partial Fulfillment of the Requirements

for the Degree of

Doctor of Philosophy

in

Applied Mathematics and Statistics

Stony Brook University

May 2014

Stony Brook University

The Graduate School

Hyoungkeun Kim

We, the dissertation committee for the above candidate for the Doctor of Philosophy degree, hereby recommend acceptance of this dissertation.

Roman V. Samulyak – Dissertation Advisor
Department of Applied Mathematics and Statistics, Stony Brook University

James Glimm – Chairperson of Defense
Department of Applied Mathematics and Statistics, Stony Brook Univeristy

Xiangmin Jiao
Department of Applied Mathematics and Statistics, Stony Brook University

Michael Zingale
Department of Physics and Astronomy, Stony Brook University

This dissertation is accepted by the Graduate School.

Charles Taber
Dean of the Graduate School

Abstract of the Dissertation

Models and Numerical Algorithms for Hydrodynamics with Atomic Processes and High Energy Density Applications

by

Hyoungkeun Kim

Doctor of Philosophy

in

Applied Mathematics and Statistics

Stony Brook University

2014

The main goal of the research is the development of numerical equation of state model enabling hydrodynamic simulations of problems involving multiple ionization and it's application in the high energy density physics (HEDP) such as the plasma jet driven magnetoinertial fusion (PJMIF) concept and the pellet injection in Tokamak via

simulations studies. For this goal, the mathematical models and numerical algorithms for ionization process has been developed, and they are demonstrated in several simulations with productive result.

A numerical model for an average ionization equation-of-state (EOS) for high-Z plasmas undergoing multiple ionization processes has been developed by improving the classical Zeldovich model. The corresponding software library has been implemented in FronTier, a hydrodynamic code that explicitly tracks material interfaces via the front tracking method. Implementation required an efficient coupling of the EOS model with Riemann solver algorithms used in high resolution hyperbolic solvers. By partially replacing costly nonlinear solvers with precomputed data sets, we were able to speedup computations by two orders of magnitude. The EOS model was verified with respect to a standard benchmark problem involving solutions of coupled systems of Saha equations.

The FronTier code with this EOS model has been used for simulations of formation and implosion of plasma liners in the concept of PJMIF. The PJMIF is an alternative method proposed to combine features of the inertial and magnetic confinement nuclear fusion to

solve the standoff problem. We performed modeling and simulations of processes relevant to PJMIF and investigated the effect of atomic processes and the internal structure of plasma liner during self-implosion. In idealized simulations of plasma liners and targets in spherical symmetry, we analyzed the liner efficiency, target compression rates, fusion energy gains, and quantified the effect of atomic processes on the liner and target compression. In 2-dimensional (2D) and 3-dimensional (3D) simulations of plasma jets merger, a cascade of oblique shock waves was observed in the merger process of discrete plasma jets. This observation explained the structure of plasma liners and agreed well with theoretical analysis.

Spherically-symmetric simulations of the pellet ablation in tokamaks, a nuclear fusion device based on magnetic confinement, have also been performed using the FronTier code equipped with the EOS for atomic processes. The pellet injection into tokamaks is proposed as a very efficient method for the fusion fuel supply and the plasma disruption mitigation. We performed studies of the ablation rate and the properties of ablation flow using our numerical tool. For more accuracy in the low temperature region, we up-

graded the average ionization model by including the continuum assumption of statistical weights of ionization level. The ablation rate of neon and argon pellets decreased due to ionization-induced energy sinks, and the ablation flow reached a multi-transonic state similar to that observed in deuterium pellets.

To my parents and wife

Contents

List of Figures

List of Tables

Acknowledgements

I would like to express my profound gratitude to my advisor, Doctor Roman V. Samulyak, for his advice, surpport and guidance toward my Ph. D. degree. He has taught me not only the way to do the research of scientific computation, but also the way to become a professional scientist. He is my lifetime role model.

I would like to thank Doctor James Glimm, Doctor Xiangmin Jiao, and Doctor Michael Zingale for being my dissertation committee members. I also deeply appreciate the infrastructure by them, without which my previous research might be impossible.

I would like to thank Dortor Kyewon Koh Park and Dortor Seungsul Park for their support and advice when I was in Ajou University. I could have an opportunity to study abroad because of their enormous help.

I would also like to thank our research group members and all friends in AMS for their friendship and encouragement during my five years study as a graduate student at Stony Brook. It has been my great happiness and honor

to have so many brilliant friends in this period. In particular, I would like to mention Lina Zhang, my collaborator for joint project. Her limitless effort for research always has inspired me to work very hard and enabled the successful result.

Throughout my academic career, the constant support of my parents and my wife has always motivated me to go forward. Regardless of the physical distance between us, my parants always have given their unconditional love. Without my wife, Aram Kim, I could never have been able to finish my Ph. D. degree. She always has been my mentor and support me to overcome many difficulties. My dissertation is dedicated to them.

During the years for Ph. D. degree at Stony Brook, I have gone through many beautiful and exciting research experiences. I am really grateful to have gone through them, and I look forward to what comes next. I thank all people who have help me through this fantastic journey.

Chapter 1

Introduction and Motivation

The high energy density physics (HEDP) spanning various physics areas including astrophysics and nuclear fusion application, has drawn many theoritical, numerical and experimental studies for long time. In the numerical work of HEDP, one of the important factors is a reasonable model for the atomic processes such as dissociation and ionization because it can change a simulation result significantly. We have developed the hydrodynamic system with enhanced algorithm for atomic processes using the FronTier code.

The system of hydrodynamic equations called the Euler equations, contains the conservation equations of mass, momemtum, and energy with the equation-

of-state (EOS) which charaterize the fluid material:

$$\frac{\partial \rho}{\partial t} = -\nabla \cdot (\rho \mathbf{u}), \tag{1.1}$$

$$\rho \left(\frac{\partial}{\partial t} + \mathbf{u} \cdot \nabla \right) \mathbf{u} = -\nabla P, \tag{1.2}$$

$$\rho \left(\frac{\partial}{\partial t} + \mathbf{u} \cdot \nabla \right) e = -P \nabla \cdot \mathbf{u} - \nabla \cdot \mathbf{q}, \tag{1.3}$$

$$P = P(\rho, e) \tag{1.4}$$

where ρ, $\mathbf{u}$, e, and P are density, velocity, specific internal energy, and pressure, respectively. In the modeling of pellet injection in Tokamak, the term $(-\nabla \cdot \mathbf{q})$ described the external heat source of hot electrons streaming along magnetic field line into the ablation cloud.

1.1 Modeling of Atomic Physics Processes in Equation-of-State

The constitutive relation, or EOS, decribes the thermodynamics of fluids and gases and closes the system of Euler equations 1.1. Accurate EOS modeling based on thermodynamic theory is important because it affects the dynamics of fluid flow. In the case of plasma jets, most of previous simulation works [7,8] have used polytropic gas EOS for partially ionized gas with altered γ (adiabatic exponent) value to mimic the ionized state of gas. This approach clearly has various limitations to obtain an accurate simulation result because the changed γ value is not an correct value for ionized gas and the dynamics

of atomic processes such as dissociation and ionization is not captured at all. This restriction motivates the development of EOS models for partially ionized gas. The energy sink induced by atomic processes in the partially ionized gas definitely influences the thermodynamic properties of fluid such as pressure, γ, sound speed, ... etc.

For deuterium plasmas, the plasma EOS in [9] was used to resolve the dissociation and ionization processes and for high-Z atom plasma, the numerical EOS in [10] was developed by us based on the average ionization method (AIM) in [11]. Both EOS models assume local thermodynamic equilibrium and the assumption was verified in specific cases. In the simulation of plasma jets and ablation cloud of pellet derived from the application to nuclear fusion, the atomic processes had changed the simulation results significantly compared to the case using polytropic EOS. For instant, the energy sink caused by atomic processes produced more nuclear fusion efficiency in the PJMIF and mutiple transonic flow in the simulation of pellet injection in Tokamak.

1.2 Plasma Jets Driven Magneto-Inertial Fusion

Nuclear fusion is a nuclear reaction in which two or more atomic nuclei merge to produce a new type of atomic nucleus. During this fusion process, high energy is required to overcome the electrostatic repulsive force between nuclei. There are the magnetic confinement fusion (MCF) and the inertial confinement

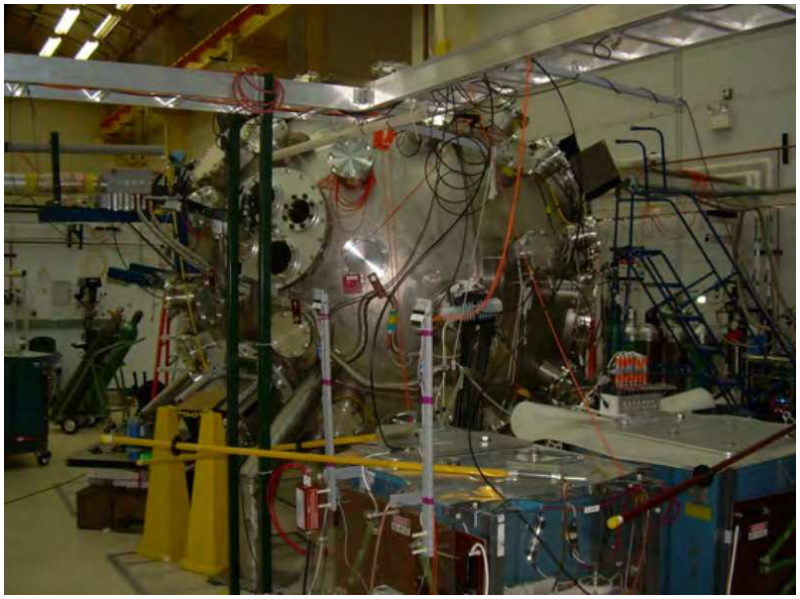

Figure 1.1: Picture of PLX chamber at LANL. Taken from [1].

fusion (ICF) depending on the confinement methods. The magnetized inertial fusion (MIF) [12], a hybrid method of MCF and ICF was proposed for more efficiency as well as the reduction of nuclear fusion cost. The PJMIF by Thio *et al.* [13] is a one of the methods for magnetized inertial nuclear fusion by using a spherical array of supersonic plasma jets. In this method, a plasma liner is formed from merger of discrete plasma jets launched from the periphery of the implosion chamber and used to implode the central magnetized target. This method is proposed to solve the stand-off problem for protection of hardwares from implosion as well as the reduction of their manufacturing cost. More specific review of PJMIF is in chapter 3.

Several theoretical and numerical works on the fusion energy gain, the stagnation pressure, the deconfinement time, and the hydrodynamic efficiency of PJMIF [6,14,15] have been reported. Th hydrodynamic efficiency is a ratio

of kinetic energy of plasam liner to fusion energy gain and the deconfinement time is the duration between the time of the peak pressure and the time when the peak pressure is decreased by the factor of two. The stagnation pressure is the maximum pressure during implosion of plasma liner on plasma target. The fusion gain scaling laws comparing with theoretical predictions are also studied. In [7, 16], the simulation of the self-collapse of argon liners using the parameters from the Plasma Liner Experiment(PLX) at Los Alamos National Laboratory (LANL), were performed by including the radiation effect. In these works, the radiation effect in front of the plasma liner reduced a pressure of vacuum region and increased the efficiency of plasma liner significantly. The picture of PLX chamber at LANL is shown in Figure 1.1. And the PLX plans to merge 30 plasma jets with high density and high Mach number to study the self-collapse, and implosion on solid and gas targets.

However, most of previous numerical works for PJMIF employed the approximated γ value to mimic the atomic processes and were on spherically symmetric 1D liners. In [10], the Mach number of plasma liners in PJMIF was increased by including atomic processes via plasma EOS models and various important charateristics of PJMIF such as nuclear fusion efficiency have changed. In [17], more realistic 3D simulation of plasma jets merger had performed and explained via the cascade of oblique shock waves. The lowered efficiency of imploding plasma liners has been quantified numerically for the first time and the different dynamics of plasma jets through oblique shock waves has been produced because of atomic processes during plasma jets merger.

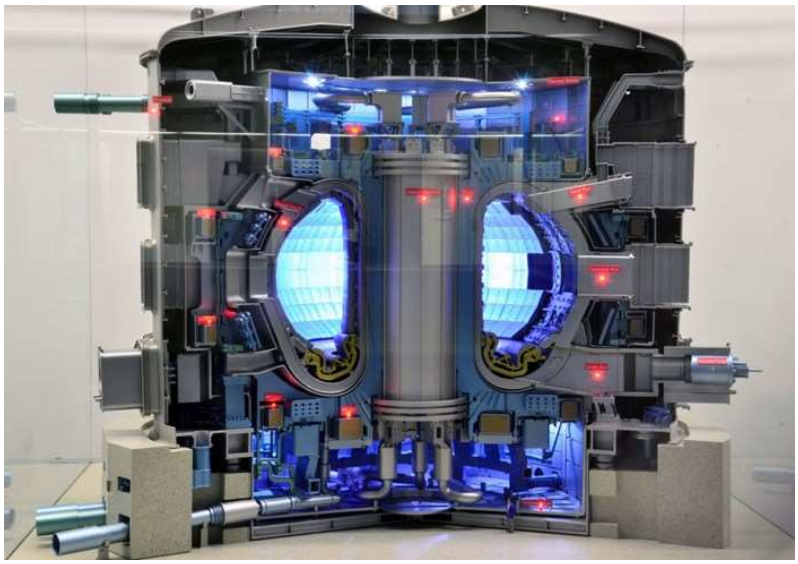

Figure 1.2: Picture of ITER. Taken from [2].

1.3 Pellet Ablation in Thermonuclear Fusion Devices

An experimentally proven method of refueling tokamaks is by pellet injection [18, 19]. Pellet penetration well inside plasma of tokamak has enabled the plasma to exceed the empirical density limit [20], which is of importance to the next generation tokamak such as the International Thermonuclear Experimental Reactor (ITER). Pellet injection is currently seen as the most likely refueling technique for ITER [21]. Furthermore, the injection of killer pellets which is an impurity pellet has been suggested as a method for fast shutdown of large tokamaks [22] without causing serious damage to the tokamak machine. Thus it is imperative that pellet injection phenomena be understood via simulations before very expensive experiments are undertaken in ITER shown in Figure

1.2. The resolution of complex physics processes in flows of liquids and weakly ionized plasmas inside tokamak plasmas is of major importance for full scale tokamak modeling in the presence of fueling processes, disruption mitigation techniques etc. Such flows are usually characterized by significantly different spatial and/or temporal scales compared to the main characteristic scales of a fusion device, as well as significantly different physical properties compared to the tokamak plasma. Mathematical approximations used in fusion plasma models and implemented in plasma MHD codes are not appropriate for such subscale flows, hence essentially new mathematical models and numerical tools are required [9, 23, 24].

As a frozen pellet of deuterium or high-Z atoms is injected into the hot plasma tokamak fusion reactor, it is rapidly heated by long mean-free-path electrons streaming along magnetic field lines, leading to ablation at the frozen pellet surface, with a shield of neutral gas and an ionized high density plasma cloud around it. This can trigger magnetohydrodynamics (MHD) instabilities [25]. In [25], the internal dynamics of plasma cloud was resolved without the details of pellet ablation and realistic pellet parameters. An improvement of such large scale simulations was obtained by Samtaney et al. [26] using an MHD code based on the Chombo AMR package [27]. For the pellet ablation, the Chombo MHD code used an analytical neutral gas shielding(NGS) model, describing the ablation as a moving density source. Parks [28] theoretically explained the motion across flux surfaces using arguments such as curvature and E×B drifts.

The ablation process involves complex interactions between the partially

conducting ablation cloud, the background plasma and magnetic field, and the motion of the pellet itself. The ablation of tokamak pellets and its influence on the tokamak plasma have been studied using several approaches. Among the pellet ablation models, a semi-analytical neutral gas shielding (NGS) model by Parks and Turnbull [29] has achieved a significant success in explaining experimental data. This 1D steady state hydrodynamics model provides the scaling of the ablation rate with respect to the pellet radius, plasma temperature and plasma density. However, it neglects MHD, geometric effects, and atomic effects such as dissociation and ionization. Theoretical studies of the magnetic field distortion [30], equilibrium pellet shape under high ablation pressures [31], radial displacement of the pellet ablation material [28, 32], and cloud oscillation [33] have also been performed.

A detailed investigation of the ablation process including the dissociation, ionization and the non-local electron heating of the pellet cloud was simulated with two dimensional hydrodynamics, i.e., the background plasma and magnetic field were stationary [34, 35]. More recently, two-dimensional hydrodynamic simulations have been performed that include solid-to-gas phase transition treatment, dissociation, ionization, and a kinetic heat flux model. These simulations showed the presence of shocks in the pellet cloud as well as the flattening of the pellet due to fluidization, which can shorten the pellet lifetime by as much as a factor of three if the pellet is assumed to be rigid and stationary [23]. More improved 2D simulations with the MHD effects and detailed atomic physics processes in the ablation cloud were reported in [9, 24].

Previous simulation studies, focusing on the fueling application of pellets,

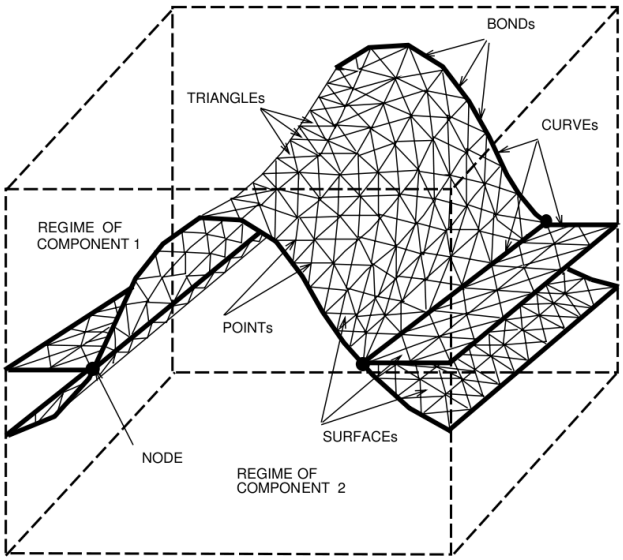

Figure 1.3: Schematic picture of front tracking method. Taken from [3].

have limited the choice of the pellet material to deuterium. However high-Z pellets have a potential for other important tokamak applications, in particular the plasma disruption mitigation. In this work, we provide results of numerical studies of the ablation of argon and neon pellets and compare them with theoretical predictions and studies of deuterium pellets. Simulations have been performed in the 1D spherically-symmetric approximation using the hydrodynamic code FronTier [36] with recently developed physics models for the pellet ablation such as the electronic heat flux model and the numerical EOS with the support for multiple ionization of high-Z gases [10].

1.4 FronTier code

The FronTier code [36] is a hybrid Lagrangian-Eulerian code based on the front tracking method [3]. The front tracking method tracks dynamically moving fronts (interfaces between materials) which are Lagrangian meshes moving through a volume filling Eulerian grid, shown in Figure 1.3. The front tracking method significantly reduces numerical diffusion across interfaces and the multiphase simulation by applying different numerical models to materials seperated by explicit interfaces. For example, different EOS models can be applied into subdomains separated by interfaces to resolve the properties of materials in each sections. The FronTier code with this front tracking method can evolve and resolve topological changes of a large number of interfaces in 2-dimensional (2D) and 3-dimensional (3D) spaces, and the dynamics of interfaces is determined by the Riemann problem for the systems of conservation equations. For the interior solvers, the FronTier code has equipped with the high order shock capturing schemes such as the Monotonic Upstream-centered Scheme for Conservation Laws (MUSCL) [37]. Currently, the FronTier code supports compressible and incompressible Navier-Stokes equations with phase transitions, MHD equations in the low magnetic Reynolds number approximation [38], and oil reservoir equations. The FronTier code has been used on various supercomputers for the several simulations (Rayleigh Taylor instability, turbulent fluid mixing, liquid accelerator targets, pellet injection in Tokamak, diesel fuel jet, etc.) [6, 9, 10, 17].

In all simulations of this dissertation, we use the MUSCL scheme which is

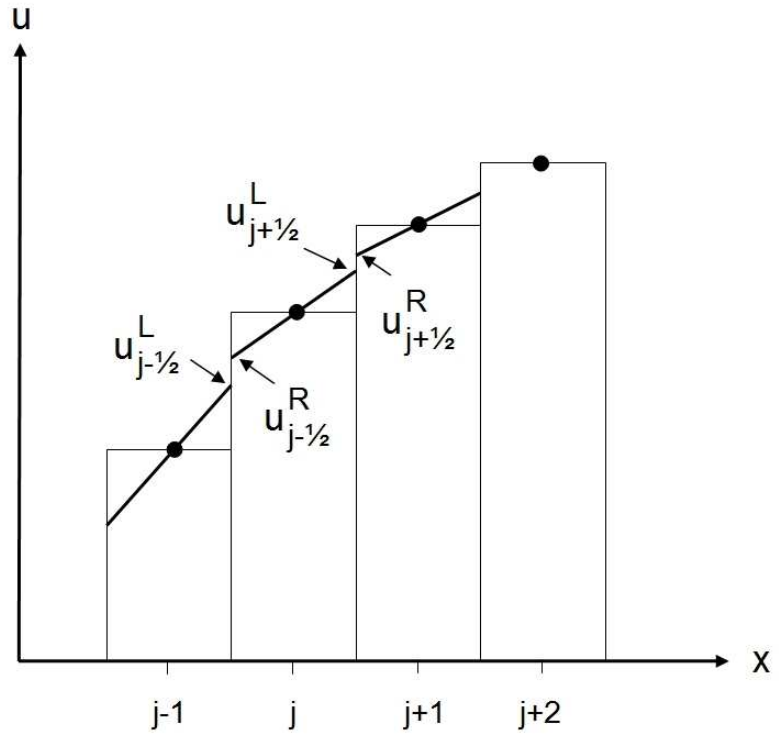

Figure 1.4: Schematic picture of the MUSCL scheme. Taken from [4].

a finite volume method with second order of accuracy in space. This scheme is derived based on the Godunov's scheme by converting the piecewise constant approximation to reconstructed states at the cell boundary, shown in Figure 1.4. After solving Riemann problem with reconstructed states, the interior states are updated based on fluxes across the cell edges.

As the ability to accurately resolve strong spherical shock is central to the application in HEDP such as plasma jet driven magnetoinertial fusion (PJMIF), the verification tests and their comparison with analytic solutions to the Noh problem [39] have been performed. In the Noh problem, a gas is initialized with uniform states of density, pressure, and radially inward velocity. A shock forms at the origin and propagates outward as the gas stagnates. An identical verification test was performed in [7] and [8] for the Raven, Hellios, and SPH codes.

The problem of interest contains an infinite, isotropic, zero temperature ideal gas with uniform initial velocity directed radially inward to the center. A shock wave is generated at the origin at the initial time, shown in 1.5. As the shock wave propagates outward, the state behind the shock remains constant. For the $\gamma = 5/3$ gas with the initial density $\rho_0 = 0.0166\, kg/m^3$ and velocity $v_0 = -100\, km/s$, the state behind the shock is as follows [39]:

$$\begin{aligned} \rho_s &= \rho_0 \left(\frac{\gamma+1}{\gamma-1}\right)^3 = 64\rho_0 = 1.06\, kg/m^3, \\ P_s &= \rho_0 v_0^2 \frac{(\gamma+1)^3}{2(\gamma-1)^2} = \frac{64}{3}\rho_0 v_0^2 = 3.54 \times 10^9\, Pa, \qquad (1.5) \\ v_s &= -\frac{1}{2} v_0 (\gamma - 1) = 33.33\, km/s, \qquad (1.6) \end{aligned}$$

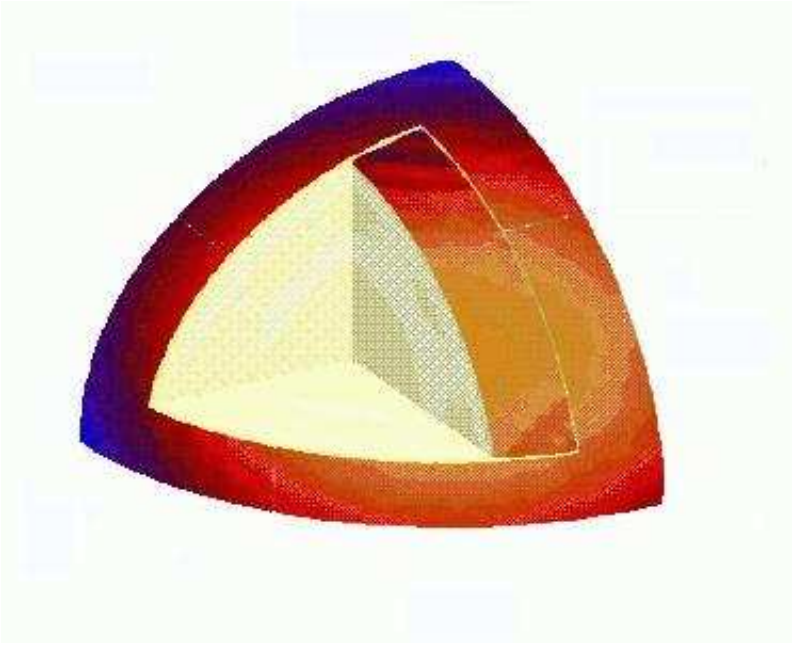

Figure 1.5: Schematic picture of 3D Noh problem. Taken from [5].

where v_s is the shock speed. The length (radius) of the simulation domain was chosen to be 25 cm, and five grid resolutions were used. The MUSCL scheme of the FronTier code is used with reflecting boundary at origin and flowing boundary at outer bound in 1D spherically symmetric domain. Table 1 summarizes the average density and pressure values, relative errors (in the L_2-norm), and the convergence rate. The convergence rate R is defined as

$$R = \log\left(\frac{\| e_{n+1} \|}{\| e_n \|}\right) \Big/ \log\left(\frac{h_{n+1}}{h_n}\right),$$

where e_{n+1} and e_n are error vectors corresponding to the grid spacing h_{n+1} and h_n.

The code verification has been performed through the comparison with the

Mesh size	1000	2000	3000	4000	5000
Density, g/cc	8.8049e-4	9.5124e-4	9.8666e-4	1.e-3	1.e-3
Pressure, bar	3.0694e4	3.3000e4	3.4101e4	3.4523e4	3.4888e4
Density Error	0.0528	0.0243	0.0146	0.0104	7.8e-3
Pressure Error	0.0369	0.0133	0.0058	0.0034	1.8e-3
Convergence Rate	N/A	1.5	2.05	1.86	2.85

Table 1.1: Mesh convergence of solutions of 1-dimensional (1D) spherically symmetric Noh problem.

Raven code [7] and the Helios code [40] which are the 1D lagrangian hydrodynamic codes. The FronTier code has obtained second or higher order convergence with the mesh refinement, which outperforms the Smoothed-particle hydrodynamics (SPH) code [8] and Raven code and is identical in accuracy to the Helios code. The main property and advantage of the FronTier code is it's ability to resolve large discontinuities across material interfaces via the method of front tracking. When there are contact discontinuities, the accuracy of FronTier code exceeds the accuracy of untracked schemes and this is critical ability for the simulation of interaction between target and liner in PJMIF.

1.5 Thesis structure

We present the development of numerical EOS model for partially ionized high-Z gas based on the average ionization method [11] in chapter 2. Using this EOS model, the simualtion work of PJMIF is provided in chapter 3. We have resolved the influence of atomic processes in the implosion of plasma liner and the merging process of discrete plasma jets via the cascade of oblique shock waves. In chapter 4, the simulation study of pellet injection into Tokamak with

the plasma EOS model is discussed. The atomic processes in the ablation flow and it's effect on ablation rate have been analysed and estimated. The on-going and future research work with summary of previous result are addressed in chapter 5.

This dissertation includes: (a) development of numerical plasma EOS model for high-Z gas; (b) verification of high-Z plasma EOS model (joint work with L. Zhang); (c) 1D simulation of plasma liner (joint work with L. Zhang); (d) 3D simulation of plasma jets merger and 3D data analysis; (e) 2D simulation of plasma jets merger and verification using oblique shock theory; (f) visualization of large 3D data using remote parallel VisIt [41]; (g) Simulation of two jets merger and validation using the result from PLX at LANL (joint work with L. Zhang); (h) 1D simulation of high-Z pellet injection in spherically symmetric domain.

Chapter 2

Modeling of Atomic Physics Processes in Equation of State

2.1 Main Hydro- and Thermodynamic Relations

The relation of $e = e(V, S)$ where e is the specific internal energy, S is the specific entropy and $V = 1/\rho$ is the specific volume, contains the thermodynamic properties of a material. The terminology for various derivatives of e are explained in detail in [42] and the basic relations are shown here for completeness.

The first derivatives of e produce the pressure $P = P(V, S)$ and the tem-

perature $T = T(V, S)$ are:

$$P(V,S) = -\left.\frac{\partial e}{\partial V}\right|_S \text{ and } T(V,S) = \left.\frac{\partial e}{\partial S}\right|_V \tag{2.1}$$

which are consistent with the fundamental thermodynamics identity of

$$de = -PdV + TdS. \tag{2.2}$$

There are the directly measurable quantities such as: the specific heats at constant volume and pressure,

$$C_V = T\left.\frac{\partial S}{\partial T}\right|_V \text{ and } C_P = T\left.\frac{\partial S}{\partial T}\right|_P, \tag{2.3}$$

the isentropic and isothermal compressibilities,

$$K_S = -\frac{1}{V}\left.\frac{\partial V}{\partial P}\right|_S \text{ and } K_T = -\frac{1}{V}\left.\frac{\partial V}{\partial P}\right|_T, \tag{2.4}$$

and the coefficient of thermal expansion,

$$\beta = \frac{1}{V}\left.\frac{\partial V}{\partial T}\right|_P. \tag{2.5}$$

The convenient dimensionless quantities (γ: adiabatic exponent and Γ: Grüneisian coefficient) can be obtained based on the second derivatives of E

as:

$$\gamma = \frac{V}{P}\frac{\partial^2 e}{\partial V^2}\bigg|_S = \frac{1}{PK_S}, \tag{2.6}$$

$$\Gamma = -\frac{V}{T}\frac{\partial^2 e}{\partial S \partial V} = \frac{\beta V}{C_V K_T}. \tag{2.7}$$

Another important dimensionless quantity, called the fundamental derivative, based on a third derivative of E is:

$$\mathcal{G} = -\frac{1}{2}V\frac{\partial^3 e/\partial V^3|_S}{\partial^2 e/\partial V^2|_S}. \tag{2.8}$$

These dimensionless quantities can be used for explanation of properties of isentropes. In cases of γ and Γ, from the following relations:

$$\gamma = -\frac{V}{P}\frac{\partial P}{\partial V}\bigg|_S = -\frac{\partial \log P}{\partial \log V}\bigg|_S \text{ and } \Gamma = -\frac{V}{T}\frac{\partial T}{\partial V}\bigg|_S = -\frac{\partial \log T}{\partial \log V}\bigg|_S, \tag{2.9}$$

the isentrope near V_0 can be approximated as:

$$P \approx P_0\left[\frac{V}{V_0}\right]^{-\gamma} \text{ and } T \approx T_0\left[\frac{V}{V_0}\right]^{-\Gamma}. \tag{2.10}$$

In case of the fundamental derivative, from the following expression:

$$\mathcal{G} = -\frac{1}{2}V\frac{\partial^2 P/\partial V^2|_S}{\partial P/\partial V|_S} = \frac{1}{2}\frac{V^2}{\gamma P}\frac{\partial^2 P}{\partial V^2}\bigg|_S, \tag{2.11}$$

the convexity of the isentropes in the P-V plane can be estimated by using $\mathcal{G}$.

In application to fluid dynamics, these dimensionless quantities (γ, Γ, g,

and $\mathcal{G}$) play a vital role. For example, the adiabatic exponent γ is a dimensionless sound speed ($\gamma = c^2/PV$) and the criteria of these values determine the characteristics of the system such as strictly hyperbolic.

In the polytropic gas, the $PV = RT$ for specific gas constant R is obtained from the fundamental thermodynamic identity of 2.2 and the experiments of Boyle and of Joule-Thompson. The measurable quantities are expressed by the ratio of specific heats ($\gamma_0 = C_P/C_V$) as following:

$$C_V = \frac{1}{\gamma_0 - 1}R, \quad C_P = \frac{\gamma_0}{\gamma_0 - 1}R, \tag{2.12}$$

$$K_S = \frac{1}{\gamma_0 P}, \quad K_T = \frac{1}{P}, \quad \beta = \frac{1}{T}. \tag{2.13}$$

From these quantites, the dimensionless quantites are $\gamma = \gamma_0$, $\Gamma = \gamma_0 - 1$, and $g = \gamma_0 - 1$. In this case, $e = C_V T$ and $S = C_V \ln(TV^{\gamma_0 - 1}) + Constant$. So the equation of state is:

$$e = e_0 \left[\frac{V}{V_0}\right]^{\gamma_0 - 1} \exp\left[(\gamma_0 - 1)\frac{S}{R}\right] \tag{2.14}$$

with some constants of E_0 and V_0.

2.2 Equation of State for Deuterium

In [9], the plasma EOS model for deuterium and its numerical implementation was introduced. The main result is represented here for completeness. For a partially dissociated and partially ionized deuterium gas, the pressure and

specific internal energy are expressed as

$$P = \left(\frac{1}{2} + \frac{1}{2}f_d + f_i\right)\frac{\rho k T}{m_a} \tag{2.15}$$

$$e = \left(\frac{1 - f_d}{2(\gamma_m - 1)} + \frac{f_d + f_i}{\gamma - 1}\right)\frac{kT}{m_a} + \frac{1}{2}f_d\frac{k\epsilon_d}{m_a} + f_i\frac{k\epsilon_i}{m_a}, \tag{2.16}$$

where γ_m and $\gamma = 5/3$ are specific heat ratios for molecules and atoms, respectively, k is the Boltzmann constant, m_a is the mass of the atom(ion). The dissociation fraction is $f_d(\rho, T) = (n_a + n_i)/n$ and ionization fraction is $f_i(\rho, T) = n_i/n$ where the total number density of *nuclei* is $n \equiv 2n_g + n_a + n_i = \rho/m_a$ and the number density of D_2 molecules, D atoms, and D^+ ions are n_g, n_a, and n_i. By using the Saha equations [11], the dissociation and ionization fractions can be calculated with the dissociation energy ($\epsilon_d = 4.48$ eV) and the ionization energy ($\epsilon_i = 13.6$ eV). The Saha equations for deuterium are (in eV units):

$$\frac{f_i^2}{1 - f_i} = 3.0 \times 10^{21}\frac{T^{\alpha_i}}{n}\exp\left(-\frac{\epsilon_i}{T}\right), \tag{2.17}$$

$$\frac{f_d^2}{1 - f_d} = 1.55 \times 10^{24}\frac{T^{\alpha_d}}{n}\exp\left(-\frac{\epsilon_d}{T}\right), \tag{2.18}$$

where $\alpha_i = 3/2$ and the parameter α_d is selected to be 0.327 for the best approximation of deuterium thermodynamic data [43].

2.3 Equation of State for High-Z Gases

The numerical EOS model for partially ionized high-Z gas has been developed based on the average ionization method in [11]. For the completeness, we provide a derivation of the average ionization method in the following.

Suppose a high-Z monatomic gas can achieve multiply ionized states with the ionization energies $I_1,\ I_2, \ldots, I_Z$. The pressure and specific internal energy can be written as

$$P = (1+f_e)\,\frac{\rho kT}{m_a} \tag{2.19}$$

$$e = \frac{3}{2}(1+f_e)\,\frac{kT}{m_a} + \frac{1}{m_a}\sum Q_m f_m + \frac{1}{m_a}\sum W_m f_m, \tag{2.20}$$

where f_e and f_m are fractions of electrons and ions with the ionization degree m, $Q_m = I_1 + I_2 + \ldots + I_m$ is the energy required to remove m electrons, I_m is m-th ionization potential, and W_m is the electronic excitation function. There are the conservation laws for f_m and f_e expressed as $\sum_m f_m = 1$ and $\sum_m m f_m = f_e$. These f_m and f_e can be calculated from the system of Saha equations under the assumption of local thermodynamic equilibrium

$$\frac{f_{m+1} f_e}{f_m} = \frac{2m}{\rho}\frac{u_{m+1}}{u_m}\left(\frac{2\pi m_e kT}{h^2}\right)^{3/2}\exp\left(-\frac{I_{m+1}}{kT}\right), \quad m = 1, \ldots, Z, \tag{2.21}$$

where h: Planck constant and u_m: electron partition functions. Because of expensive computation cost for the coupled system of Z nonlinear equations (2.21), it is almost impossible to solve this in hydrodynamic simulation. To reduce the computational cost, the AIM is introduced in [11]. In this method,

the continuum approximation of the ionization fractions, particle number densities, and the ionization energy function is introduced as:

$$f_m \to f(m), \quad n_m \to n(m), \quad I_m \to I(m).$$

The integral forms of conservation laws are

$$\int n(m)dm = n,$$

$$\int m\, n(m)dm = n_e$$

. Then a single ordinary differential equation is derived from the coupled system of Saha equation:

$$\left(1 + \frac{d\log n}{dm}\right) n_e = AT^{3/2} \exp - \frac{I(m+1)}{kT}. \tag{2.22}$$

The continuum representation of the argon ionization energies, shown in Figure 2.1, was obtained using a third order piece-wise polynomial approximation and the discrete energy spectrum of the argon atom.

The distribution of ionized states $n(m)$ at given density and temperature values resembles a sharp, Gaussian-type curve centered at the average ionization $\bar{m}$ defined as

$$\bar{m} = \frac{\int m\, n(m)dm}{\int n(m)dm} = \frac{n_e}{n} = m|_{\frac{dn}{dm}=0}\,.$$

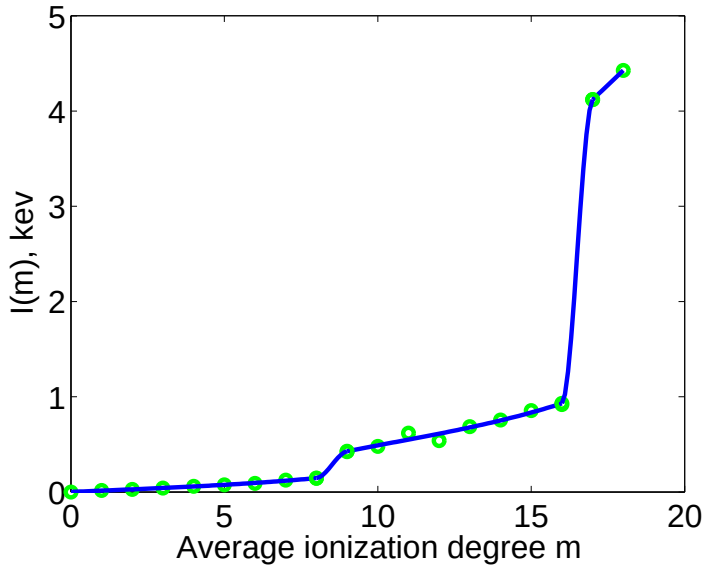

Figure 2.1: Ionization energies of argon atom (circles) and their continuum representation by function $I(m)$ (solid line). (Joint Work with L. Zhang)

From (2.22), the average ionization value is

$$\bar{m} = \frac{AT^{3/2}}{n} \exp -\frac{\bar{I}}{kT}. \tag{2.23}$$

The corresponding internal energy and pressure for average ionization modeling are

$$P = n\,(1+\bar{m})\,kT \tag{2.24}$$

$$E = \frac{3}{2}\,(1+\bar{m})\,\frac{kT}{m_a} + \frac{1}{m_a} Q(\bar{m}), \tag{2.25}$$

Following [11], we use the average ionization value for the calculation of thermodynamic quantities. Substituting (2.24) or (2.25) into the Saha equation(2.26) with the discrete functions I_m and Q_m replaced by the corresponding

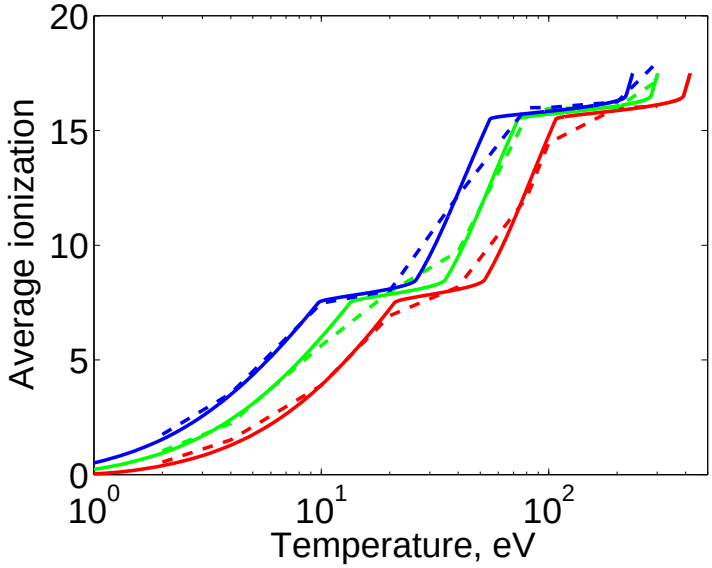

Figure 2.2: Comparison of the average ionization calculated using the Zeldovich model (solid lines) and the full system of coupled Saha equations (dashed lines) at given temperature and three density values, $5 \times 10^{-3}\, g/cm^3$ (red bottom lines), $5 \times 10^{-5}\, g/cm^3$ (green middle lines), and $5 \times 10^{-7}\, g/cm^3$, (blue top lines) is shown. (Joint Work with L. Zhang)

continuum functions describing specific material, we obtain a single nonlinear equation for finding $\bar{m}$ at given values of specific internal energy or pressure with value of density. Using the expression for entropy from [11] and the local gamma-law fit for other thermodynamic properties, we calculate the sound speed and other quantities required by the Riemann solver.

The verification of this numerical EOS model in the FronTier code has been performed by comparing with numerical solutions of the coupled system of Saha equations. In Figure 2.2, we plot the dependence of the average ionization level of argon gas on temperature for three density values: $5 \times 10^{-7}\, g/cm^3$, $5 \times 10^{-5}\, g/cm^3$, and $5 \times 10^{-3}\, g/cm^3$. In the point of hydrodynamic states,

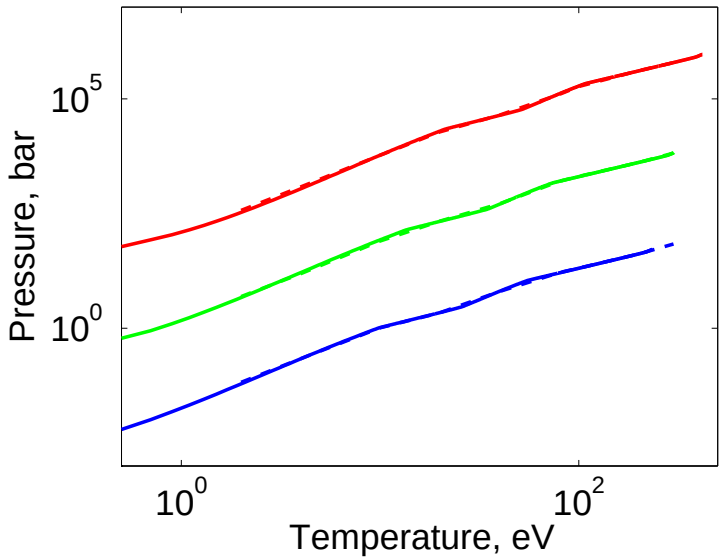

Figure 2.3: Comparison of pressure values calculated using the Zeldovich model (solid lines) and the full system of coupled Saha equations (dashed lines). Temperature dependence of the argon gas pressure at three density values, $5 \times 10^{-3}\, g/cm^3$ (top lines), $5 \times 10^{-5}\, g/cm^3$ (middle lines), and $5 \times 10^{-7}\, g/cm^3$, (bottom lines) is shown. (Joint Work with L. Zhang)

the small deviation of ionization level near non-smooth part of the graph has negligibly small influence. The corresponding pressure curves obtained using the average ionization EOS model and the coupled system of discrete Saha equations are depicted in Figure 2.3 for the same values of density.

This model is sufficiently accurate in the high energy regime. However, as it is shown in Figure 2.4, the accuracy is reduced at low temperatures corresponding to the average ionization level of order ($\overline{m} \sim 0.1$). The ablation cloud near the pellet surface is in weakly ionized state, and the inaccuracy of the original AIM could change the overall dynamics of ablation cloud in simulations. In this work, we improve our previous numerical EOS for high-Z gases by including the linear continuum approximation of statistical weight ratio ($\overline{u}$) shown in Figure 2.5. The equation in the improved AIM with $\overline{u}$ is:

$$\overline{m} = \overline{u}\ \frac{AT^{3/2}}{n} \exp -\frac{\overline{I}}{kT}. \tag{2.26}$$

The accuracy of this numerical EOS is increased further by using the numerical optimization of $\overline{I}$ when $\overline{m} < 1$. We use the modified $\overline{I}$ instead of the linear approximation to mimic the single electron model in the low energy regime. In this work, $\overline{I} = I_1(1 - \overline{m}^q)^{1/q}$ is used, where I_1 is the first ionization energy and q is a properly picked rational number when $\overline{m} < 1$. The result of the improved AIM is shown in the Figure 2.4.

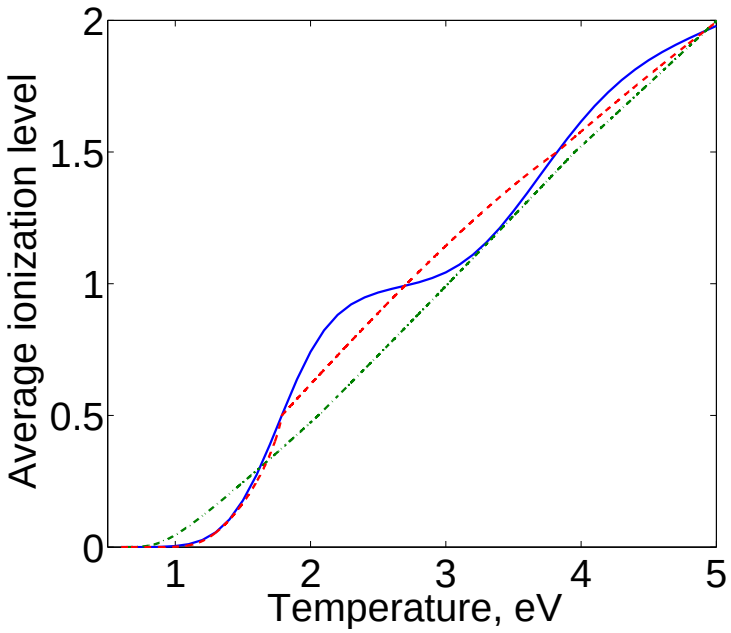

(a) Average ionization

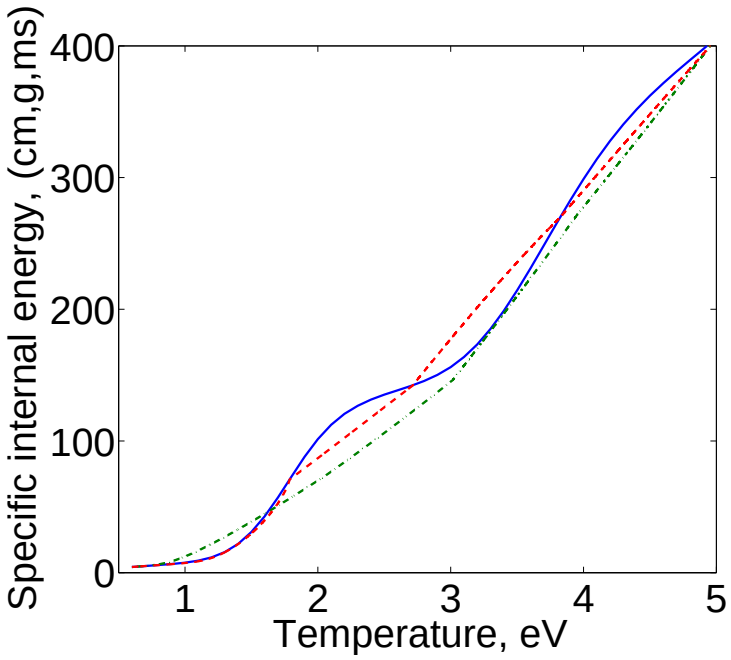

(b) Specific internal energy

Figure 2.4: The comparison of solutions from the coupled system of Saha equations (solid blue line), the original average ionization model (green dash-dotted line), and the improved average ionization model (red dashed line) for neon with density of $3.351 \times 10^{-5}\ g/cm^3$.

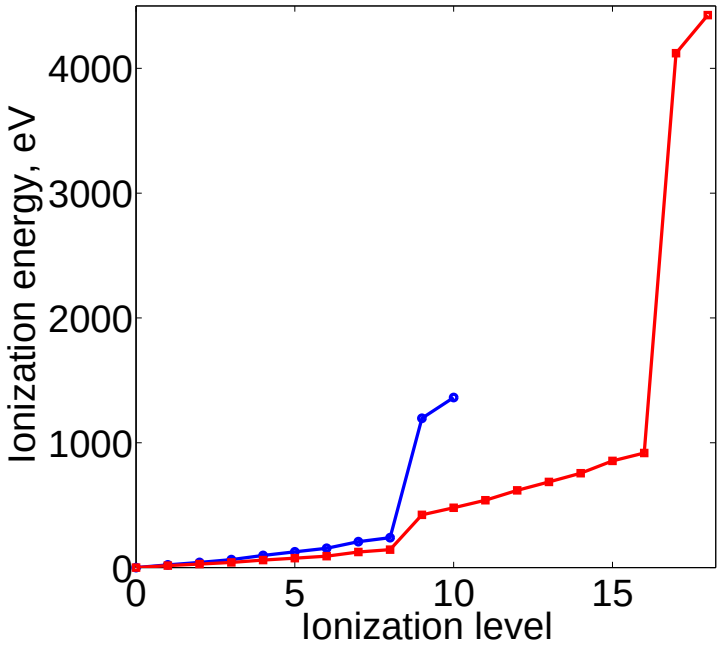

(a) Ionization energy, $\overline{I}$

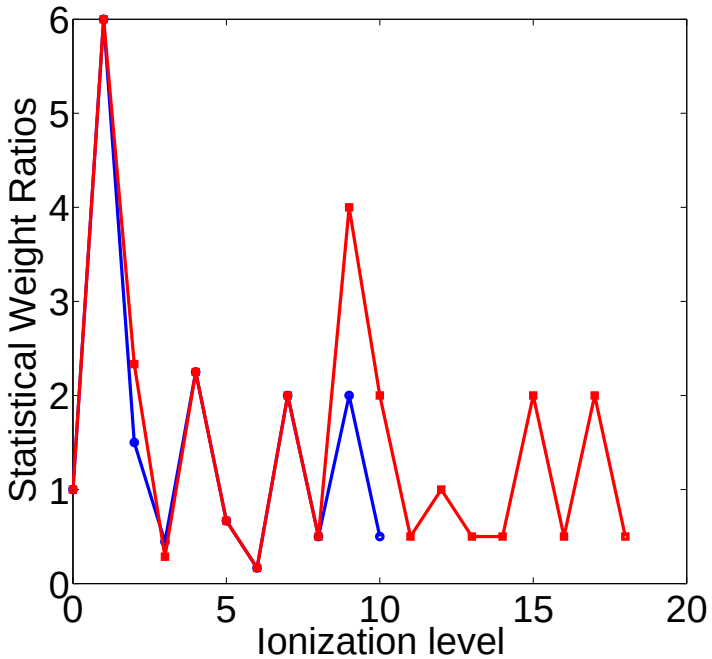

(b) Statistical weight ratios, $\overline{u}$

Figure 2.5: Ionization energy and statistical weight ratios of neon (blue-circle) and argon (red-square)

2.4 Efficient EOS Coupling with Hyperbolic Solvers

The FronTier uses the second order hyperbolic solvers such as MUSCL, that calculate conservative fluxes (density(ρ), momentum($m = \rho v$), internal energy(e)) using solutions of the Riemann problem. The variables for the Riemann problem are (density ρ, velocity v, pressure P) and we need a variable conversion which is usually difficult in the complex EOS model.

To support the hyperbolic solvers in FronTier code, several functions are developed and implemented inside of EOS files. For the EOS of ideal gas, pressure value can be obtained from specific internal energy and density ($P = (\gamma_0 - 1)E/V$) and there are simple analytic solutions for various thermodynamic quantities along characteristic line, which are required in the advanced numerical discretization algorithms, including second order MUSCL type schemes and interface propagation algorithms implemented in the FronTier code [44]. However, there are not simple formulas in the EOS with atomic processes and the nonlinear equations have to be solved to obtain the quanities required by the hyperbolic solvers.

In the case of EOS for deuterium gas, the disociation and ionization fraction are the basic variables which determine most of thermodyanamic quantities such as pressure (2.15) and specific internal energy (2.16) during the hydrodynamic simulation. To find pressure as a function of density and specific internal energy, we solve the quadratic equations (2.17) - (2.18) for f_i and f_d respectively. Substituting these solutions into the energy equation (2.16), a

nonlinear equation $\Phi(\rho, E, T) = 0$ is obtained which can be solved for T for given values of ρ and E. Then this temperature value is used to calculate the dissociation and ionization fractions and the pressure.

The basis variable in the EOS for partially ionized high-Z gas is the average ionization level $\bar{m}$ obtained from (2.26). Most of the thermodynamic quantities during hydrodynamic simualtion are determined via the value of $\bar{m}$. With the temperature value and density, the $\bar{m}$ is determined by solving the nonlinear equation (2.26) and this is used to obtain other values such as sound speed and local gamma. When we have the value of pressure or specific internal energy value, this equation (2.26) can be solved after substitution of temperature value using (2.24) or (2.25). This substitution can be applied into the other cases of Hugoniot equation and isentropic condition.

The most expensive part in the EOS for deuterium and high-Z gas is the numerical integration along a characteristic line in the isentropic gas flow. The value of $\int_{P0}^{Pstar} \left.\frac{dP}{\rho c}\right|_S$ is the integration value under constant entropy. This value is calculated frequently in the riemann solver which is one of the most fundamental routines in MUSCL type scheme. Although the direct calculation can be used in the 1D simulation, it is almost impossible to use it in the higher dimensional simulation. In [9], the tabulated data on the space of entropy and pressure was developed and used successfully. And this data set also are generated and used in the case of EOS for high-Z gas. In the data set over a space of pressure and entropy, the grid for entropy values is evenly distributed while the grid for pressure is placed logarithmically because of the rapidly changing property of inside function, $\left.\frac{dP}{\rho c}\right|_S$.

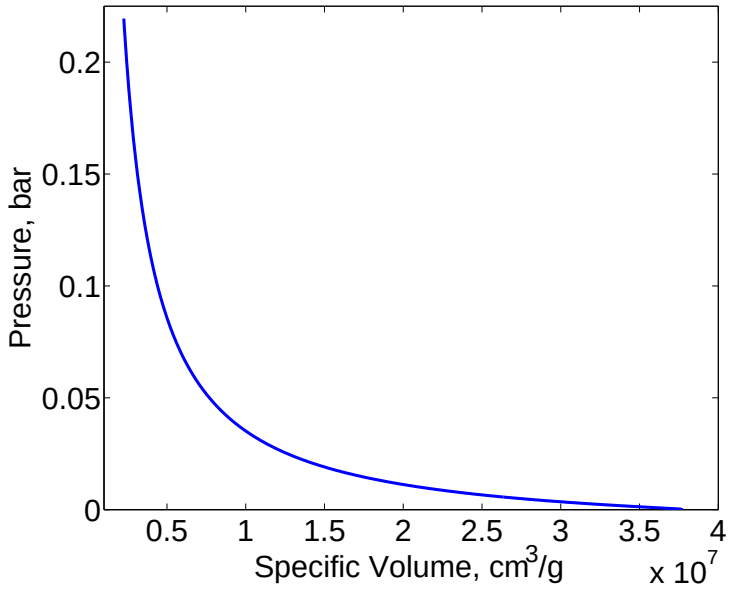

Figure 2.6: Hugoniot locus in the P-V plane

To check the Riemann problem for interacting shock waves, the Hugoniot locus is analysed [42]. The Hugoniot locus is the solution set of the equation of $h(V, S) = 0$ where $h(V, S)$ is the Hugoniot function by:

$$h(V, S) \quad = \quad E(V, S) - E_0 + \frac{1}{2}[P(V, S) + P_0](V - V_0).$$

With $(P_0, V_0) = (0.222, 2.236e6)$ in (g,cm,ms) system, the Hugoniot locus of plasma EOS for high-Z monatomic gas is shown in Figure 2.6. In this case, the uniqueness of the Riemann problem is guaranted because of convexity of the Hugoniot locus [42].

Chapter 3

Plasma Jet Driven Magneto-Inertial Fusion

3.1 Introduction

Recently, there are numerous theoretical, simulation, and experimental works about the imploding plasma liner which is formed by the merger of high Mach number plasma jets [13, 16] in the context of HEDP and the magnetoinertial nuclear fusion. The schematic picture of this concept is shown in Figure 3.1. The dynamics of a spherically symmetric liner which is imploding on a deuterium plasma target and going through the self-implosion, has been studied theoretically and numerically in [6–8, 10, 13, 14, 45–47]. In [6, 10, 14], the fusion energy gains at extreme initial states (Mach-60 deuterium, argon, and xenon liners) of the plasma liners have evaluated and the high-Z plasma liners with high Mach number have produced a reasonable nuclear fusion energy while a

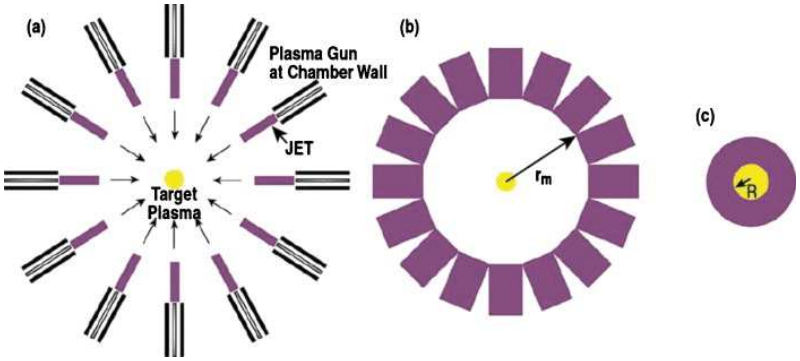

Figure 3.1: Schematic picture of PJMIF (a) Supersonic plasma jets from plasma gun. (b) Merger of discrete plasma jets at the merging radius r_m and form a plasma liner. (c) Plasma liner implodes and compresses the target. Taken from [6].

deuterium liner has not. Additionally, the properties of self-imploding plasma liners with moderate initial states which is from the PLX [45] at LANL, have checked in the works of [7, 10, 17]. The merger of 30 high-density argon jets in the Mach number range of 10 - 35, was planned in the PLX to explain the liner formation, self-implosion, and target interaction process. The PLX team at LANL has reported the experiment result of oblique merger and head-on collision of two jets [48–50]. In this section, the influence of atomic processes in plasma jets simulations, the merger process of descrete plasma jets, and the validation with PLX result are shown and explained.

3.2 Influence of Ionization on the Implosion of Plasma Liners

By using the EOS models with atomic processes such as dissociation and ionization, and the front tracking method in 1D spherically symmetric domain, the effect of atomic physics processes on the plasma liners implosion in PJMIF has been studied numerically in [10]. The initial parameters for numerical simulation of the self-collapse of the argon liners were given by the PLX at LANL.

In this section, we provide the simulation result of argon liner's implosion and the explanation of the atomic processes during the implosion. By using the 1D Lagrangian method, several simulations of argon liners' implosion with initial conditions from PLX at LANL were reported in [7, 46]. In this simulation work, the properties of the plasma liner and the suppression of high temperature in vaccuum region had revealed by including the radiation transport phenomena. But the most of simulations in [7] had employed the ideal gas EOS model and this can be a restriction for getting a more realistic simulation result and leads us to the following numerical work.

By using the plasma EOS for argon, we have done the simulation work of plasma liners implosion with the initial parameters of PLX1 and PLX2 in [7], and compared our simulation result with the result in [7]. Through this study, we have the important role of atomic processes without radiation effects and the heat conduction. By using the initial parameter of case 6 of Table II in [7], we also tried the code comparison between the FronTier code, the RAVEN

code, and the HELIOS code. The additional effect of heat conduction during the plasma liner self-implosion and the interaction between imploding plasma liner and the plasma target were also performed and discussed in [10] by using the FronTier code.

For completeness, we provide here the initial parameters of PLX 1 and PLX 2 setups from [7]. These PLX 1 and PLX 2 simulations were performed in 1D spherically symmetric domain with reflecting condition in the origin and open condition in the outer boundary, and mesh size of 0.02 cm. In Figure 3.1 b, the plasma liner at the merging radius r_m can be assumed as uniform plasma liner and initialized in 1D spherically symmetric domain. For the PLX 1 simulation, the merging radius of the argon liner is 33 cm and the liner thickness is 44.7 cm. The initial state of the PLX1 liner is uniform with the density $\rho = 6.63 \times 10^{-8}\,\mathrm{g/cm^3} = 1.0 \times 10^{15}\,\mathrm{cm^{-3}}$, temperature $T = 2.8\,\mathrm{eV} = 32480\,\mathrm{K}$, pressure $P = 0.004482\,\mathrm{bar}$, velocity $v = 50\,\mathrm{km/s}$, and Mach number $M = 14.9$. The initial states of the PLX2 liner are the same except that the thickness of the liner is 63.6 cm. Additionally, the initial state of the liner described in case 6 of Table II in [7] is also uniform with the density $\rho = 6.63 \times 10^{-7}\,\mathrm{g/cm^3} = 1.0 \times 10^{16}\,1/\mathrm{cm^3}$, temperature $T = 1.0\,\mathrm{eV} = 11604\,\mathrm{K}$, pressure $P = 0.02911\,\mathrm{bar}$, velocity $v = 50\,\mathrm{km/s}$, and the Mach number $M = 22.571$. For this case, the merging radius is 24.1 cm and the liner thickness is 25.5 cm.

Because of initial temperature which is comparable with first ionization energy level of argon, the average ionization level of the initial liner is 2.25. This initial state of ionization level has increased very slowly in the initial

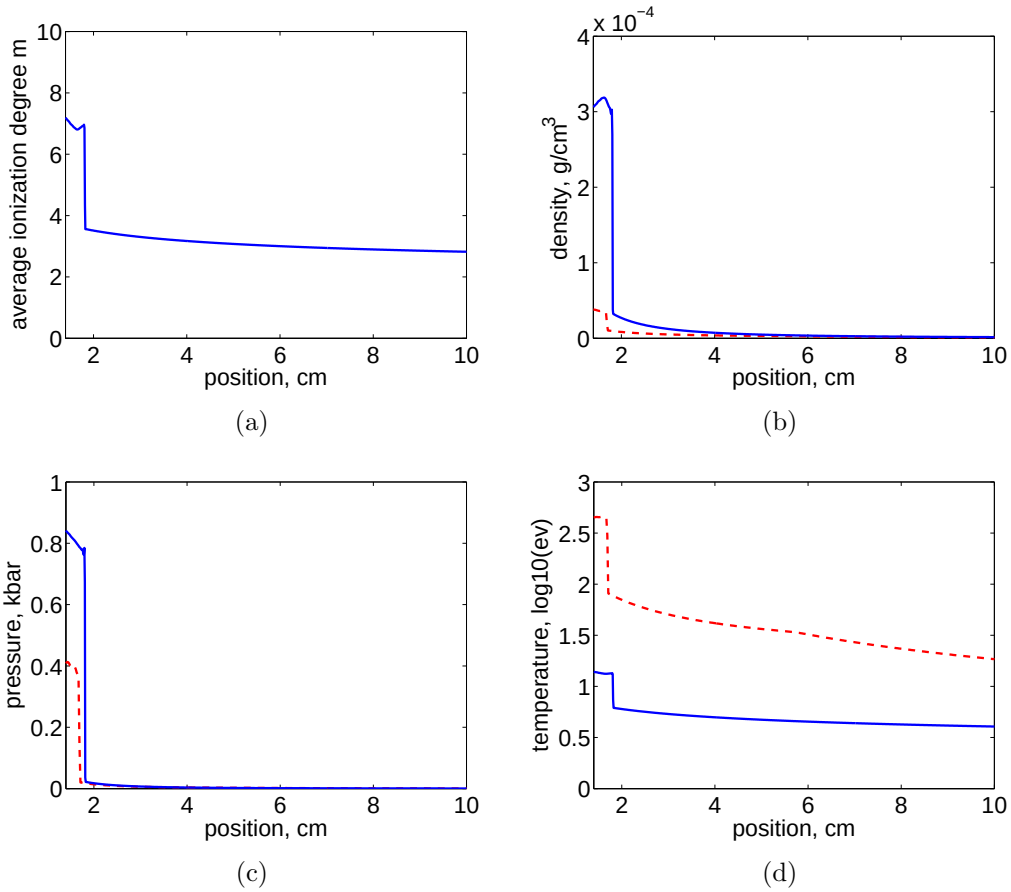

Figure 3.2: average ionization (a), density (b), pressure (c), temperature (d) of the imploding argon liners around the stagnation time with PLX 1 parameters by using plasma EOS model (blue solid line) and polytropic EOS model (red dashed line). (Joint Work with L. Zhang)

part of plasma liner self-implosion. But, in the late process of plasma liner self-implosion, the states of liner such as temperature, pressure, and average ionization level have soared abrutly. In figure 3.2(a), the average ionization across the plasma liner has depicted when the plasma liner is approaching the stagnation state. The average ionization level has increased into 7.2 near the chamber center and in figures 3.2(b) - 3.2(d), the corresponding quantities of the density, pressure, and temperature in the imploding plasma liner are shown. By comparing the simulation using the ideal EOS model, we obtained a factor of 6.5 increase of density, a factor of 2 increase of pressure, and a factor of 2.3 decrease of temperature in the center of the chamber using the plasma EOS which can resolve the ionization process. Additionally, the sound speed and the Mach number of imploding plasma liner are shown in the figure 3.3 and a factor of 1.5 increase of Mach number is obtained comparing with the case of ideal EOS model.

In Figure 3.4, the evolution profile of the maximum pressure of plasma liners has shown in the processes of self-implosion and implosion on the solid target. We obtain the higher maximum pressure in the case of plasma liner implosion on the solid target than the case of self-implosion which is caused by the effect of the imperfect vacuum condition. This vacuum condition is caused by the compressed residual gas in front of the imploding plasma liner. The residual gas in front of the imploding plasma liner is gradually suppressed and the increased pressure of this remnant gas, can degrade the efficiency of the imploding plasma liner and induce the lowered maximum pressure during self-implosion, while this effect is decreased in the case of solid target simula-

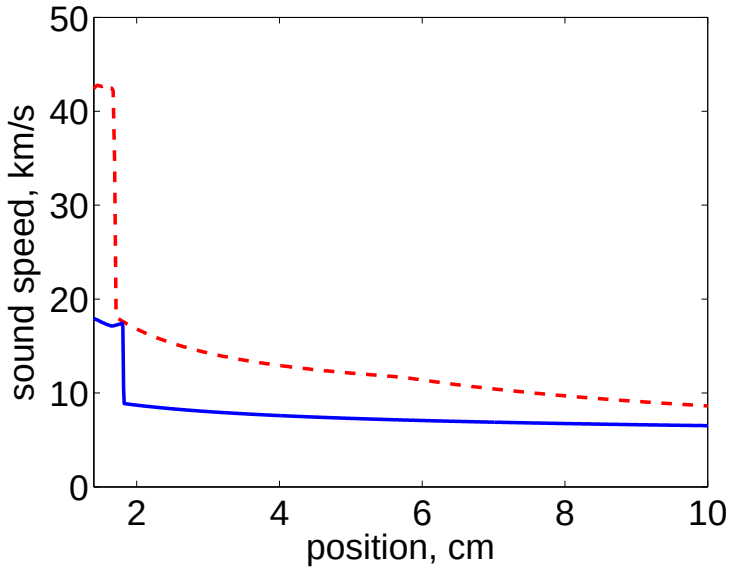

(a)

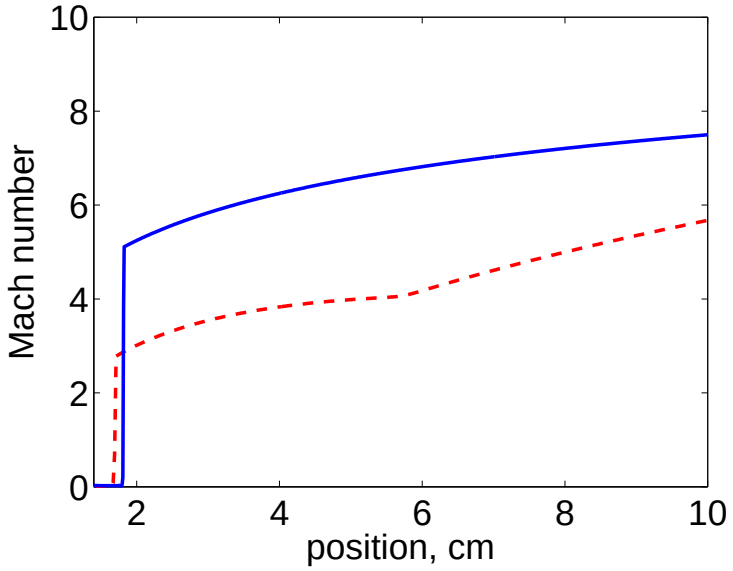

(b)

Figure 3.3: sound speed (a) and Mach number (b) of the imploding argon liners around the stagnation time with PLX 1 parameters by using plasma EOS model (blue solid line) and polytropic EOS model (red dashed line). (Joint Work with L. Zhang)

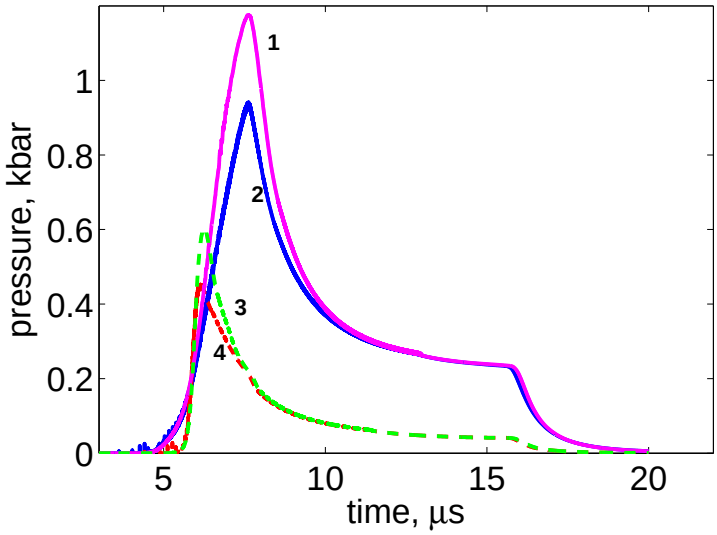

Figure 3.4: Evolution of maximum pressure by using (1) plasma EOS with 0.5 cm solid target (purple solid line), (2) plasma EOS (blue solid line), (3) polytropic EOS with 0.5 cm solid target (green dashed line) and (4) polytropic EOS (red dashed line) of imploding argon liners with PLX 1 parameters. (Maximum pressure is picked among the values near liner's leading edge.) (Joint Work with L. Zhang)

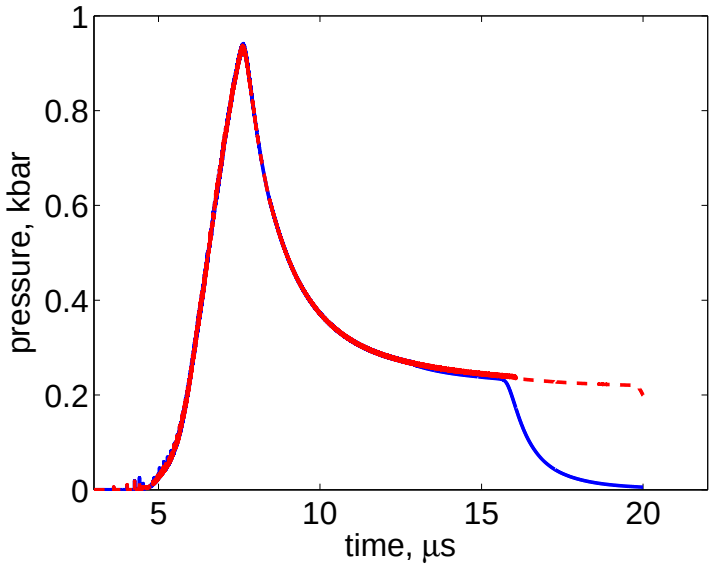

Figure 3.5: Evolution of maximum pressure of PLX1 (blue solid line) and PLX2 (red dashed line). (Joint Work with L. Zhang)

tion. In the comparison with the result in [7], the maximum pressures in this simulations are approximately three orders of magnitude lower and this big difference can be explained by the inclusion of the radiation effect. In these simulations of self-implosion and solid target interaction of plasma liners, the maximum pressure during stagnation increased by almost the factor of two when we include the atomic processes during the imploding process.

The effect of thickness of the imploding plasma liner was discussed in [6] and the result showed that it had the little effect on the plasma target compression and deconfinement time. In [6], the deconfinement time is discussed and defined as the duration between the time of the maximum compression of plasma target and the time when the peak pressure is decreased by the factor of two while there is the definition of the stagnation time in [7]. The definition

of deconfinement time in [6] was derived based on the fusion energy gain since a nuclear fusion process in the plasma target were finished 95% when the maximum pressure had decreased by the factor of two. In this work of an imploding argon liner, we also check the influence of thickness of imploding plasma liner. In Figure 3.5, the maximum pressure profiles of imploding plasma liner with PLX1 and PLX2 parameters from [7], have shown. The deconfinment times and maximum pressure profiles are almost identical in these cases of PLX1 and PLX2 which is consistent with the argument in [6]. In [7], the definition of the stagnation time was introduced to explain the self-imploding plasma liners since the PLX parameters are far below the nuclear fusion ignition conditions. The definition of the stagnation time in [7], is the time difference between the time of peak maximum pressure of self-imploding plasma liner and the time when the reflected shock wave in self-imploding plasma liner meets the trailing edge of the plasma liner and degrade the imploding efficiency. From this definition, the stagnation times have increased in the case of PLX2, which is consistent with the thickness of plasma liner with PLX2 comparing the case with PLX1. In the case of nuclear fusion study, the definition of the deconfinement time in [6] is more appropriate, while the stagnation time is relevant notion to capture the high energy density region in the case of self-imploding plasma liner. The usage of the plasma EOS in self-imploding plasma liners has a limited effect in the stagnation time because the intense ionization processes are occurred in narrow region of leading edge of plasma liners.

The simulation result using the parameters of case 6 of Table II in [7] is shown in Figure 3.6. We compare this result with Figures 5 and 12 in [7]

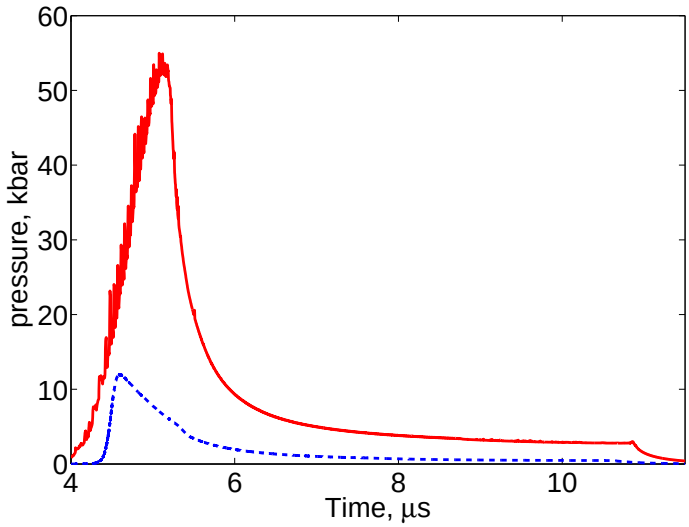

Figure 3.6: Evolution of maximum pressure of case 6 of Table II in [7] by using plasma EOS (red solid line) and polytropic EOS (blue dashed line). (Joint Work with L. Zhang)

for code comparison. By comparing the RAVEN and HELIOS codes in [7], the FronTier code with the polytropic EOS model, produced maximum pressure value between the values from other two codes. The FronTier code with LTE EOS with ionization process, produce the similar value with it from the HELIOS code with PROPACEOS non-LTE EOS in [7]. This PROPACEOS (PRism OPACity and Equation Of State code) include various atomic processes (collisional ionization, recombination, excitation, etc) for LTE plasmas and optically thin non-LTE plasmas [51]. In [46], the HELIOS code produced almost the same maximum pressure when the LTE EOS comparing to the case with non-LTE EOS. The local thermodynamic equilibrium assumption to the simulation of deuterium plasma liners is explained in [10] and this argument can also be applied to the case of argon liners since the eletron number density

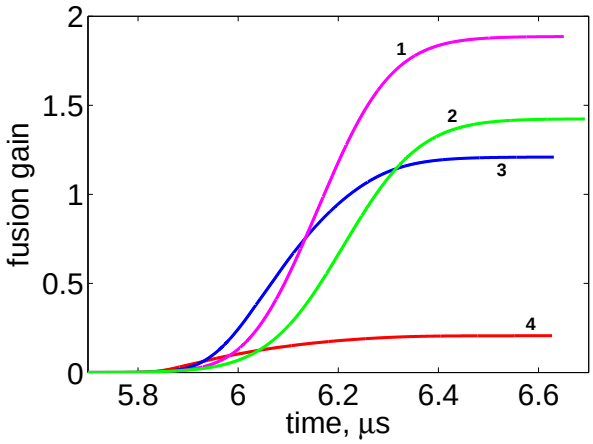

Figure 3.7: Comparison of fusion gains with different target radius using same argon liner and polytropic EOS. (target radius: 15cm(1), 20cm(2), 10cm(3), 5cm(4)) (Joint Work with L. Zhang)

is bigger than the case of deuterium plasma liners.

As the local thermodynamic equilibrium is an important assumption of the plasma EOS model, we evaluated it's applicability by analyzing thermodynamic states in the plasma liner. As the ionization fraction is almost constant and negligibly small during the liner implosion in the case of deuterium liner, we consider states of the liner close to the stagnation time, when the ionization is large and rapidly changing in time. To achieve the thermodynamic equilibrium in such a dynamic process, two conditions must be satisfied [52]: The first condition, applicable to processes at both fast and slow time scales, requires the electron number density to be higher than a critical value defined as

$$n_e \geq 7.4 \times 10^{18} \frac{z^7}{n^{17/2}} \left(\frac{kT}{E_i^z} \right)^{1/2} \ [cm^{-3}],$$

where $z = 1$ for neutrals, $z = 2$ for singly ionized atoms etc., n is the principal

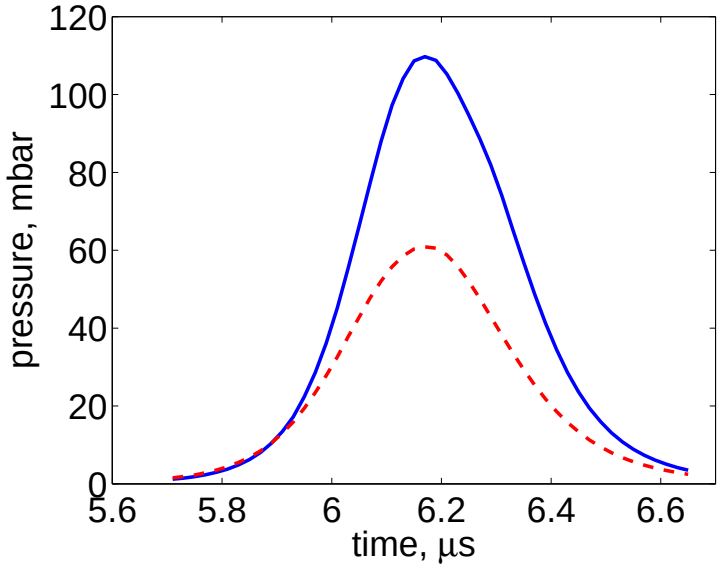

Figure 3.8: Evolution of maximum pressure with polytropic EOS (red dashed line) and plasma EOS (blue solid line) of argon liner at given time. (Joint Work with L. Zhang)

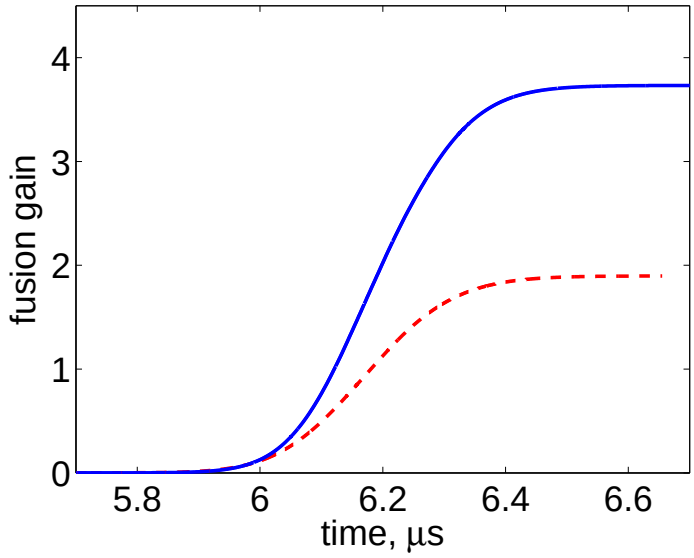

Figure 3.9: Evolution of the fusion energy of the plasma target compressed by the argon liner at given time with polytropic EOS (red dashed line) and plasma EOS (blue solid line). (Joint Work with L. Zhang)

quantum number, and E_i^z is the ionization energy. To justify the usage of the LTE EOS model in the simulation, this condition is checked. The value of critical electron number density is 1.15×10^{19} for temperatures close to the stagnation point. The actual number density of electrons according to the ionization fraction from EOS is 1.3×10^{23}, or four orders of magnitude higher. While the formula above sometimes is used for high-Z materials, it is applicable, strictly speaking, only to hydrogen and helium. The second condition defines a typical time scale for reaching the equilibrium in transient plasmas:

$$\tau \simeq \left[3 \times 10^{-7} \left(\frac{E_i}{kT} \right)^{3/2} n_e \right]^{-1} \frac{n}{n_a} \frac{M}{m} \, [sec].$$

Close to stagnation, the time scale given by this expression is $1.6 \times 10^{-12} sec$. This is approximately two times smaller than the smallest time step used during the simulation. Therefore the local thermodynamic equilibrium is established on shorter time scales than the resolved hydrodynamic time scale. This proves the applicability of our LTE EOS model.

Finally, we investigate the interaction between argon plasma liners and plasma target and the nuclear fusion efficiency in the point of plasma target radius and ionization process. We use the same liner dimensions as in [6] and the same liner particle number density as in previous simulations with xenon liners. This gives the following initial state of the argon liner: density $\rho = 4.0 \times 10^{-4} \, \mathrm{g/cm^3} = 6.03 \times 10^{18} \, 1/\mathrm{cm^3}$, temperature $T = 0.7269 \, \mathrm{eV} = 8435.15 \, \mathrm{K}$, and pressure $P = 9.35 \, \mathrm{bar}$. The heavy, high-Z liners produce more efficiency for compression of plasma target used for the deuterium liners and

the most optimal plasma target radius for xenon liner is 20 cm in [6]. Following the same procedure, the most optimal plasma target radius is found by using several target radius and the polytropic EOS model in the case of argon plasma liner. In Figure 3.7, the result is shown and the case of plasma target with the radius of 15 cm produce is most efficient with respect to the fusion gain. This radius of plasma target is used in the simulation of the effect of the ionization process on the stagnation pressure and fusion energy gain In the case using the polytropic EOS, the plasma target stagnation pressure is 61 Mbar while it has been increased into 110 Mbar when the ionization process is included in the plasma liner via plasma EOS model, shown in Figure 3.8. The fusion energy gain efficiency are 1.9 and 3.7, correspondingly, depicted in Figure 3.9.

3.3 Studies of 3D Structure of Plasma Liners

By using the FronTier code, the 3D numerical simulation of merger of argon plasma jets has been performed to analyze the internal structure and self-collapse properties of plasma liner. A cascade of oblique shock waves which are produced during the merger process of plasma jets is observed for the first time numerically in [17] and we quantify the heating of plasma liner and the decrease of plasma liner's Mach number. In the comparison with the 1D spherical symmetric simulation of plasma liner, the peak maximum pressure of 3D plasma liner during the self-implosion reduced to the ten times lower value because of the oblique shock waves and the adiabatic compression heating, although the pressure and density profiles of two cases are identical.

A factor of ten times variations of density and pressure in the leading part of the plasma liner are also obtained and this could cause the RayleighTaylor instability during the interaction with the potential plasma target.

Through the 3D merger simulation of plasma jets, the evolution of high Mach number jets which are interacting each other at the mergin radius, has checked and explained via the cascade of oblique shock waves. Because of oblique shock waves produced during the merger process of discrete plasma jets, the peak maximum pressure of self-imploding uniform plasma liners is significantly higher than the value of plasma liner from the merger of discrete jets. In this section, the plasma liner from the merger of plasma jets also has analyzed in the point of plasma target compression and the influence of oblique shock waves.

3.3.1 Initialization

The simulation result of the propagation of a single injected argon plasma jet from the nozzle of the plasma gun on the chamber wall to the chamber center, was shown here. This result of single plasma jet propagation can be used as input data for a 3D plasma jets merger simulation before the interaction of discrete plasma jets to decease the 3D computation domain. In this simulation, we use PLX case 6 of Table 2 in [7], which has the following constant states: initial velocity 50 km/s, the density $\rho = 5.747 \times 10^{-6} g/cm^3$, and the temperature $T = 1eV$. The ambient vacuum is modeled as rarefied gas with density $\rho_0 \sim 10^{-9} g/cm^3$ and pressure $\sim 10^{-6}\ bar$. In this work, the simulation

was performed in a 2D cylindrically symmetric domain with open boundary conditions and the axially symmetry of plasma jet during the propagation is assumed. The mesh size in this simulation is 0.2 cm.

The distribution of the initial density and the density at $t = 18.5\mu s$ or at 0.925m distance from the plasma gun nozzle have shown in Figure 3.10. In Figure 3.11, profiles of density, pressure, temperature and average ionization in the transverse direction through the jet center at different moments of time are depicted. In this simulation, it is observed that the all quantities decrease in time and the plasma jet is very diffusive because of expansion of the plasma jet in the vacuum chamber condition. The boundary of plasma jet is defined as the location of points with the density of $0.1\rho_0$ to preserve the notion of the expanding plasma jet.

The jet expansion can also be estimated analytically. The liner expansion model with constant initial sound speed [14] predicted the increase of the jet radius b as $b(r_m) = b_0 + c_0(r_c - r_m)/u_j$. Here b_0 is the initial jet radius, c_0 is the initial sound speed, r_c is the chamber radius, and r_m is the merging radius.

With the assumption of adiabatic expansion and sound speed decrease of jet, the linear expansion model can be expressed:

$$c(t) = \sqrt{\gamma \frac{P(t)}{\rho(t)}} = \sqrt{\gamma A \rho(t)^{\gamma-1}},$$

where A is the constant in the adiabatic relation $P = A\rho^{\gamma}$. If we assume that

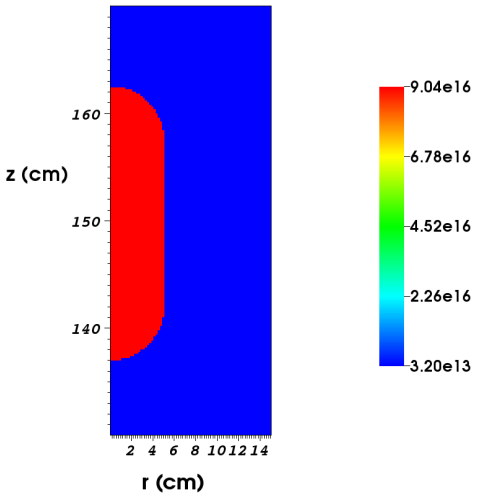

(a) t = 0.0 ms

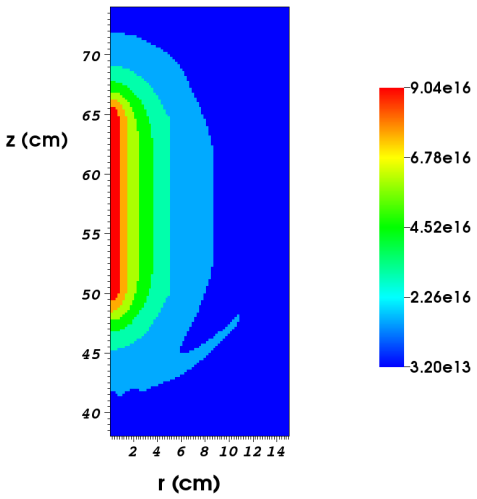

(b) t = 0.0185 ms

Figure 3.10: Density ($1/cm^3$) of the detached jet. (a): initial density; (b): density before merging radius. (Joint Work with L. Zhang)

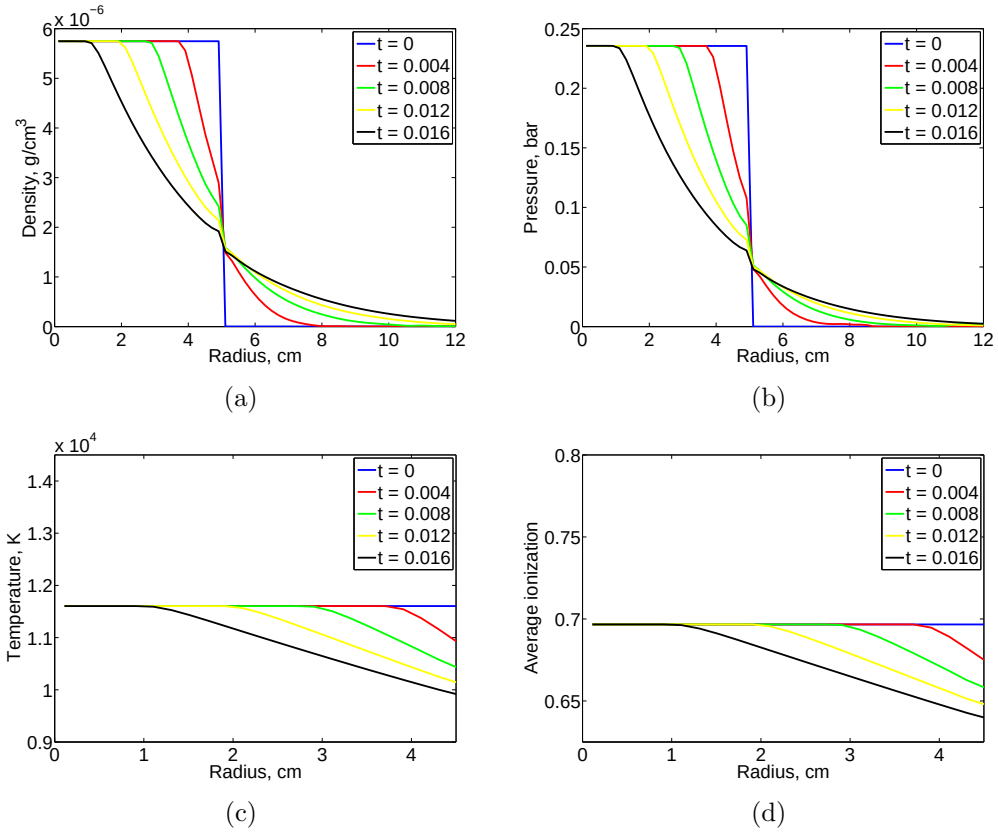

Figure 3.11: Density, pressure, temperature and average ionization across the center of the detached argon jet. (Joint Work with L. Zhang)

the jet diameter is much smaller than the jet length, we get

$$b(t) = b_0 + c_0 \left(\frac{b_0}{b(t)} \right)^{(\gamma-1)} t.$$

If the diameter is comparable to the jet length, we obtain the following relation by assuming spherical expansion

$$b(t) = b_0 + c_0 \left(\frac{b_0}{b(t)} \right)^{\frac{3}{2}(\gamma-1)} t.$$

For simulations using the argon plasma EOS, we calculate the local gamma $\gamma = 1.14$ from the simulation result and solve numerically the corresponding nonlinear equations. Figure 3.12 depicts the time dependence of the expanding jet radius from simulation and analytic model.

Because the Mach number of plasma is very important factor in the peak maximum pressure of plasma liner and the plasma target compression rates (the nuclear fusion efficiency), the evolution of Mach number during the jet expansion is one of the most important factors. In the tail of the plasma jet, there is a very strong rarefaction wave which can influence the Mach number of plasma jet. When we calculate the average Mach number of plasma jet, the high values in the tail part of plasma jet may increase the average value significantly. So we derived the new method which is appropriate into this case. In this work, the data for average Mach number value is collected from the front half of the plasma jet body.

The plasma jet cooling in the process of propagation and expansion is

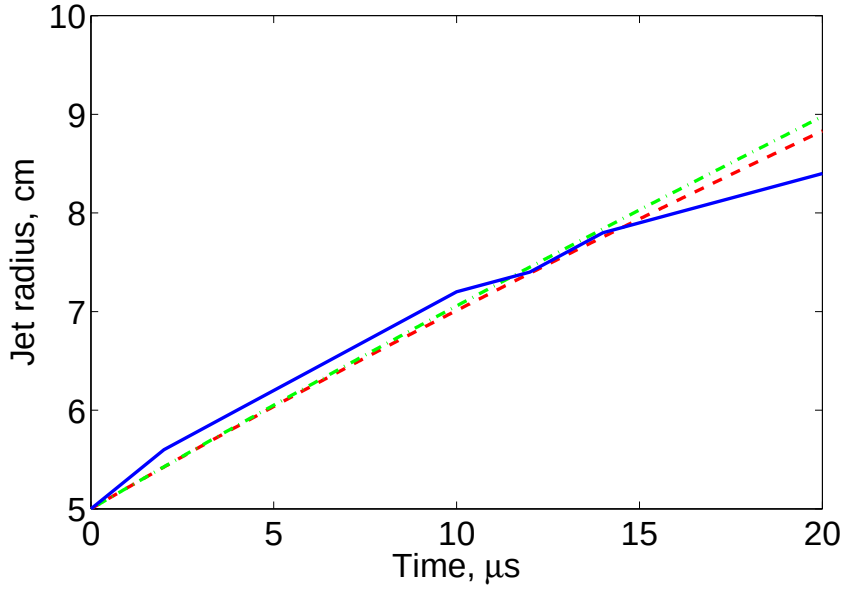

Figure 3.12: Jet expansion comparison of numerical simulation result (blue solid line), analytic model of long jet (green dash-dotted), and analytic model of short jet (red dashed line). (Joint Work with L. Zhang)

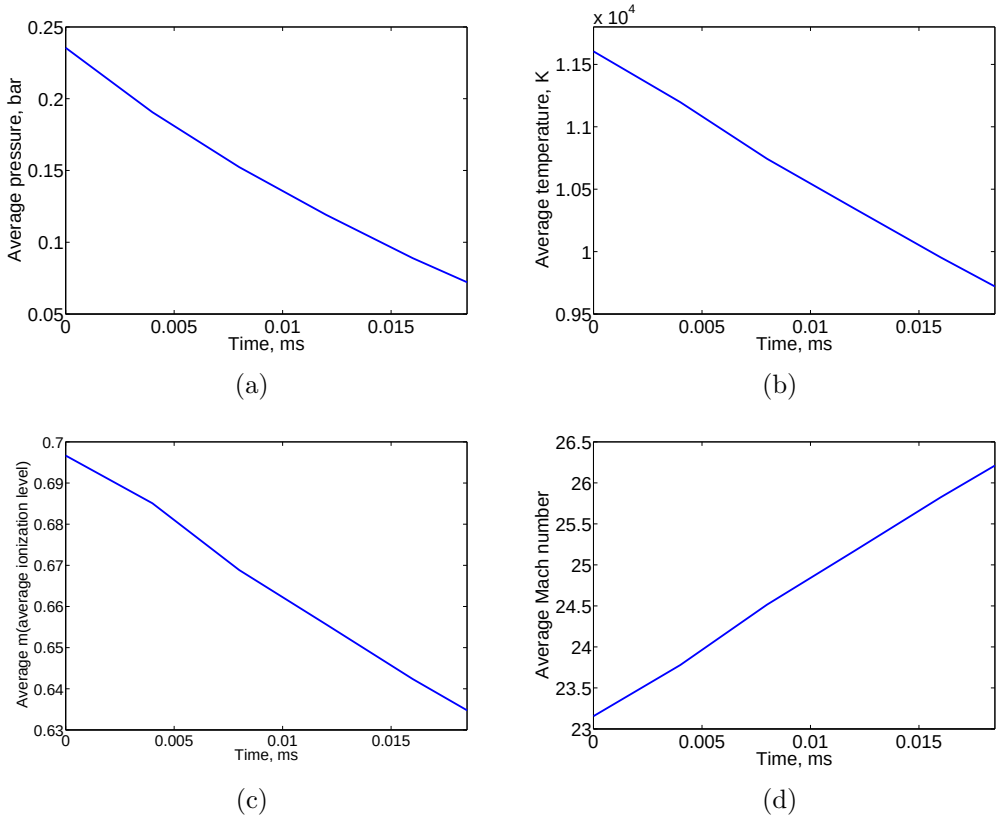

Figure 3.13: Average values of pressure, temperature, m (average ionization) and Mach number of a detached argon jet. (Joint Work with L. Zhang)

depicted in Figure 3.13. In this figure, we observed the increase of the Mach number and the decrease of average temperature with time. The average Mach number after propagation of plasma jet is caused by the expansion cooling.

3.3.2 3D Simulation of 30 Argon Jets Merger

The merger process of discrete plasma jets is studied in this section. The structure and uniformity of plasma liner which is produced through the merger of plasma jets are analyzed by using the cascade of oblique shock waves. To check the efficiency of 3D plasma liner as compressor of plasma target, the comparison with 1D spherically symmetric simulation has performed in the next section.

The initialization of a 3D simulation of 30 plasma jets merger needs the initial places of plasma jets and the initial state information of plasma jets such as pressure, density, and velocity profile. The initial places of plasma jets, equivalent with the places of plasma guns, are obtained by solving the Spherical Centroidal Voronoi Tessellation (SCVT) which is for the uniform distribution of 30 points on a sphere. The software by John Burkardt [53] that implements Qiang Du's algorithm [54], was employed to solve this SCVT problem. Although the initial places of 30 plasma jets are know from PLX at LANL **??**, we used the places from SCVT problem for the consistency with following simulation work of 90 plasma jets. By using a transformation from 2D cylindrical coordinate into 3D cartesian coordinate and a corresponding numerical data set with bi-linear interpolation, the initialization of 3D states

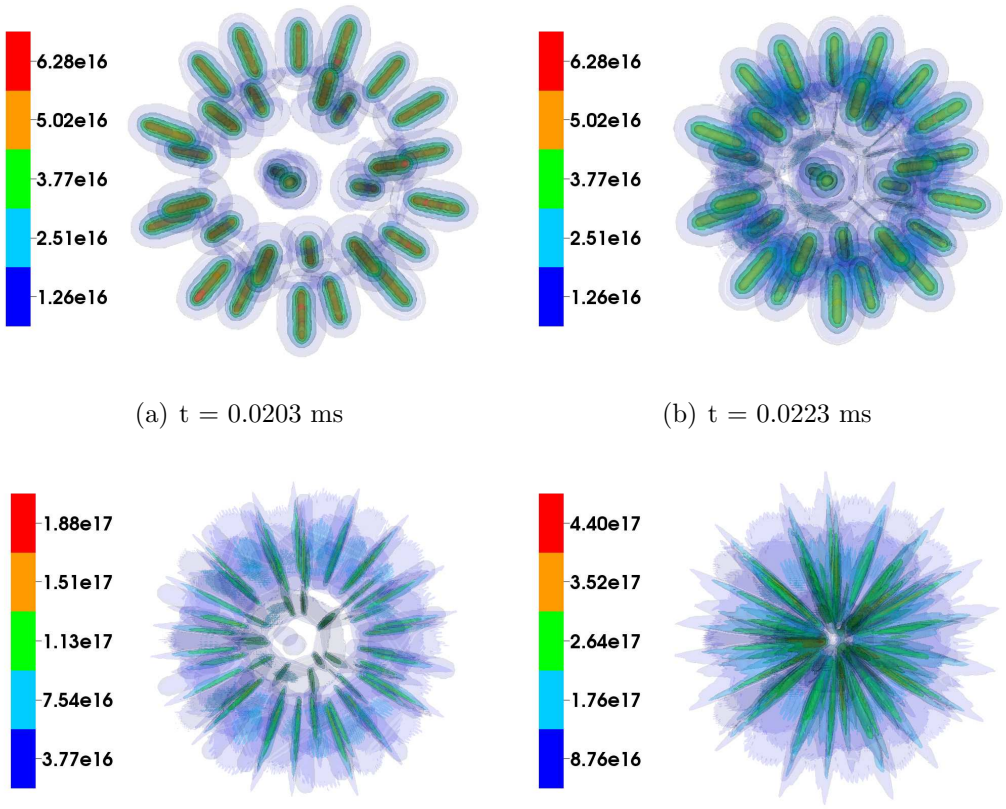

(a) t = 0.0203 ms

(b) t = 0.0223 ms

(c) t = 0.0243 ms

(d) t = 0.0263 ms

Figure 3.14: Density ($1/cm^3$) contours before merger (a, b) and after merger (c, d) of 30 argon plasma jets. (Joint Work with L. Zhang)

information of plasma jets are obtained. The open boundary condition was used and the mesh size is 0.4 cm in this 3D simulation.

Each pair of plasma jets is colliding obliquely with the angle of ~ 36 degree. The propagating plasma jets can not interpenetrate each other and are tilted via the oblique shock waves. For the verification, the mean free path of ions

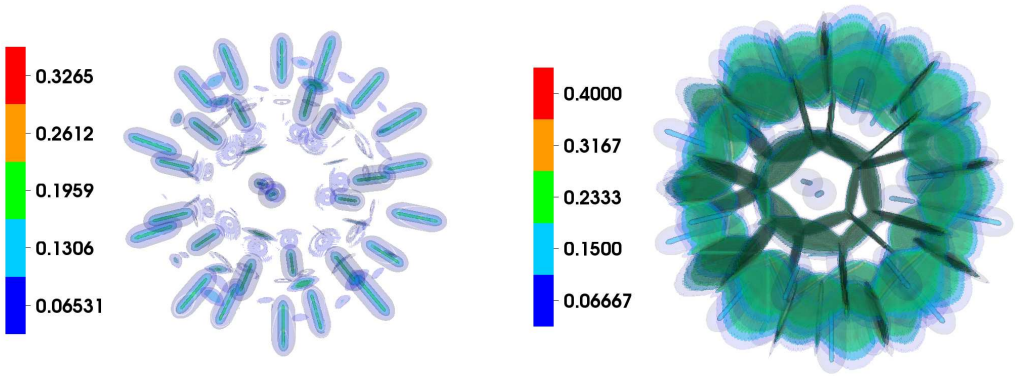

(a) t = 0.0203 ms

(b) t = 0.0223 ms

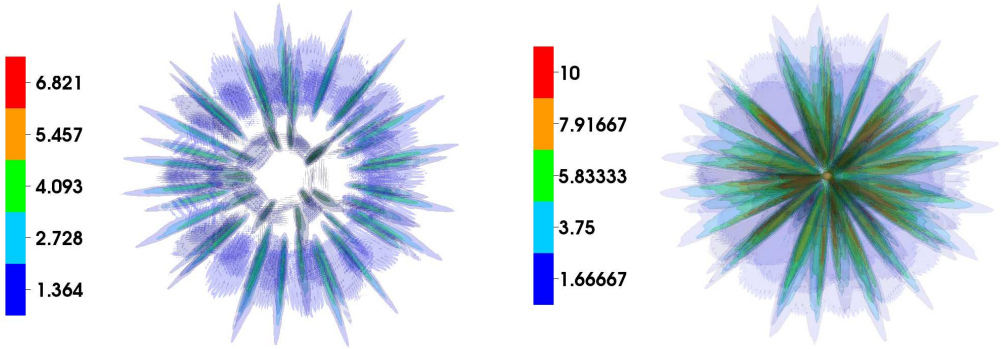

(c) t = 0.0243 ms

(d) t = 0.0263 ms

Figure 3.15: Pressure (bar) contours before merger (a, b) and after merger (c, d) of 30 argon plasma jets. (Joint Work with L. Zhang)

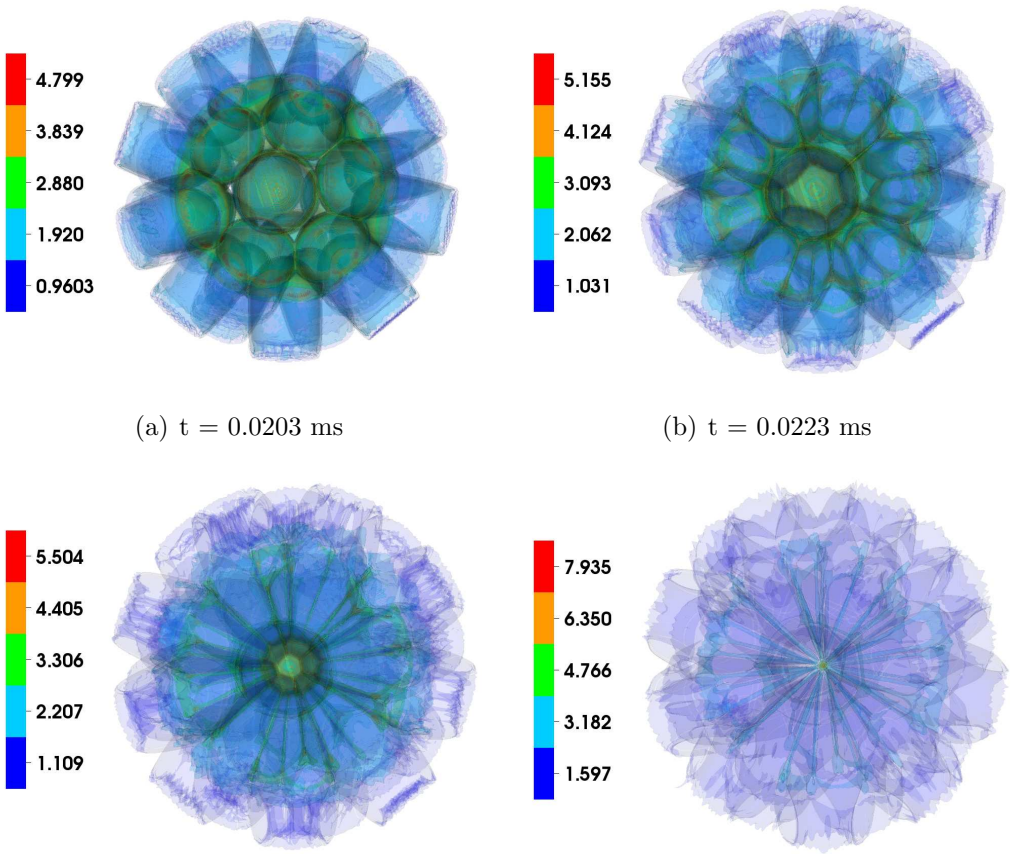

(a) t = 0.0203 ms

(b) t = 0.0223 ms

(c) t = 0.0243 ms

(d) t = 0.0263 ms

Figure 3.16: (Color online) Average ionization contours before merger (a, b) and after merger (c, d) of 30 argon plasma jets. (Joint Work with L. Zhang)

is checked. Inside the plasma jet, the mean free path is expressed [55] as

$$\lambda_i = v_{Ti}/\nu_i, \tag{3.1}$$

where the ion thermal velocity: $v_{Ti} = 9.79 \times 10^5 \mu^{-1/2} T_i^{1/2}$ cm/s, and the ion collision rate:$\nu_i = 4.80 \times 10^{-8} Z^4 \mu^{-1/2} n_i T_i^{-3/2} \ln\Lambda$, $1/s$. From the periphery of plasma jet in this work, $\mu = m_i/m_p = 40$, $T_i = 0.86$ eV, $Z \sim 1$, $n_i = 1.5 \times 10^{16}\, cm^3$, $\ln\Lambda \sim 10$, we obtain $v_{Ti} = 1.44 \times 10^5$ cm/s, $\nu_i = 1.43 \times 10^9$ 1/s, and $\lambda_i \sim 1 \times 10^{-4}$ cm. From this calculation result, it is concluded that the surface of the plasma jet is fully collisional and the center is more collisional than periphery. By using the formula about the slowing down of streaming ions on ion-ion collisions [55], we calculate the slowing down rate:

$$\frac{dv_\alpha}{dt} = -\nu_s^{\alpha\backslash\beta} v_\alpha \tag{3.2}$$

where $\nu_s^{\alpha\backslash\beta} = (1 + m_\alpha/m_\beta)\psi(x^{\alpha\backslash\beta})\nu_0^{\alpha\backslash\beta}$, $\nu_0^{\alpha\backslash\beta} = 4\pi n_\beta e_\alpha^2 e_\beta^2 \lambda_{\alpha\beta}/m_\alpha^2 v_\alpha^3$, $x^{\alpha\backslash\beta} = m_\beta v_\alpha^2/2kT_\beta$, and $\psi(x) = \frac{2}{\sqrt{\pi}} \int_0^x t^{1/2} e^{-t} dt$. Using the state of plasma jet surface and $\lambda_{\alpha\beta} \sim 10$, it is obtained that the ion's penetrating velocity ($v_\alpha^{initial} \sim 3.1 \times 10^6\ cm/s$) becomes comparable to thermal velocity after penetration distance of ~ 0.5cm. The assumption of single fluid dynamics description can be justified by considering the highly collisional property of electrons and the electrostatic interaction.

The increase of temperature, the reduction of the average Mach number, and the non-uniformity of plasma liners are caused by the cascade of oblique

shock waves. In Figures 3.14, 3.15, and 3.16, the contour of density, pressure, and average ionization level are depicted before and after merger of 30 plasma jets. The region of highest pressure is found along the place of interaction between adjacent plasma jets. Accoding to the number of neighboring plasma jets, the contour shape of high pressure is pentagon or hexagon, which is consistent with the result in [56]. Before the interaction of discrete plasma jets, the highest values of density and pressure in the plasma jet are placed in the center of plasma jets, but after the interaction, the position of highest values have changed gradually into the plane between the interacting plasma jets. In Figure 3.17(a), the density profile on plane slice of 3D plasma liner is depicted. This plane is determined by using the computational domain origin (chamber center) and two adjacent plasma jets.

3.3.3 Analysis of Oblique Shock Waves

The schematic of oblique shocks is shown in Figure 3.18(a). In this figure, δ denotes the angle between the plasma jet and the plane of reflection (the median line between two jets), and α denotes the angle of the oblique shock wave. With respect to the formation of oblique shock waves, the collision of jets is similar to the collision of a jet with a solid wall at 18-degree angle, and therefore the standard theory of oblique shock waves [57] is applicable for the description of states in the after-shock region of the jet merger process. Assuming initially non-expanding flow (with parallel stream lines) with polytropic gas properties and $\gamma = 5/3$, the oblique shock wave's angle (α), pressure

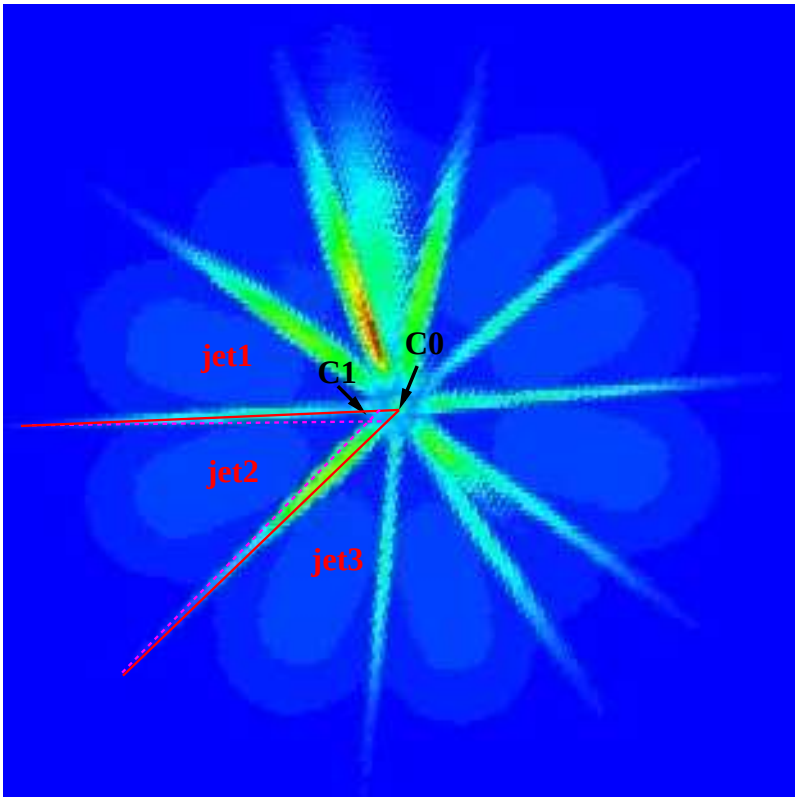

(a)

Figure 3.17: Density distribution on a slice of 3D data at stagnation. (Joint Work with L. Zhang)

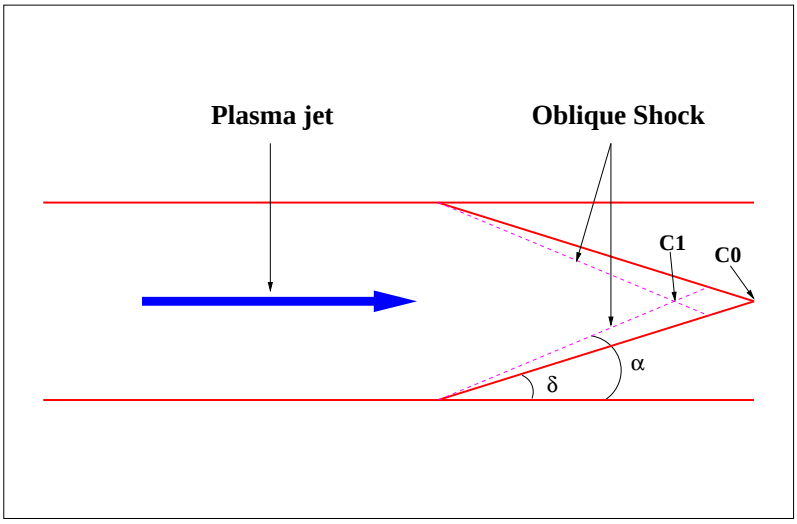

(a)

Figure 3.18: Schematic of oblique shocks in the jets merger process. (Joint Work with L. Zhang)

(P), density (ρ), temperature (T), and Mach number (M) in the after-shock region can be calculated by using following equations [58]:

$$\frac{\tan(\alpha-\delta)}{\tan\alpha} = \frac{2+(\gamma-1)M_1^2\sin^2\alpha}{(\gamma+1)M_1^2\sin^2\alpha} \tag{3.3}$$

$$\frac{P_2}{P_1} = \frac{2\gamma M_1^2\sin^2\alpha-(\gamma-1)}{\gamma+1} \tag{3.4}$$

$$\frac{\rho_2}{\rho_1} = \frac{(\gamma+1)M_1^2\sin^2\alpha}{(\gamma-1)M_1^2\sin^2\alpha+2} \tag{3.5}$$

$$\frac{T_2}{T_1} = \frac{[2\gamma M_1^2\sin^2\alpha-(\gamma-1)][(\gamma-1)M_1^2\sin^2\alpha+2]}{(\gamma+1)^2M_1^2\sin^2\alpha} \tag{3.6}$$

$$M_2^2 \sin^2(\alpha - \delta) = \frac{(\gamma - 1)M_1^2 \sin^2 \alpha + 2}{2\gamma M_1^2 \sin^2 \alpha - (\gamma - 1)} \tag{3.7}$$

where quantities with the index 1 describe the pre-shock state and the corresponding quantities with index 2 describe the post-shock state.

The simplified 2D simulations of the jet merger with the polytropic EOS is performed and compared with the oblique shock theory for better explanation of the 3D merger process of plasma jets. This 2D simulation was performed in open boundary with the mesh size of 0.1 cm. The profiles of plasma jets such as pressure, density, and velocity are initialized uniformed for comparison with oblique shock theroy. The angle between adjacent plasma jets are selected by considering the corresponding angle in the 3D plasma jets. In Figure 3.19, the density profiles at the initial and later times, are depicted. The schematic picture of first and second cascades of oblique shock waves are shown in Figure 3.19(b). In Figure 3.20, the detailed distributions of pressure, density, and Mach number after the formation of the first oblique shock waves are provided. The numerical values from simulation work in post-shock region are summarized in Table 3.1 and match well with the oblique shock theory. The discrepancy between the theory and simulation result in Table 3.1 can be explained by the steady assumption of gas flow in the oblique shock theory. In the 2D simulation, it is hard to obtain the steady state because of the cascade of oblique shock waves.

The colliding angle of neighboring plasma jets after each oblique shock waves is same because the direction of plasma jet after oblique shock wave

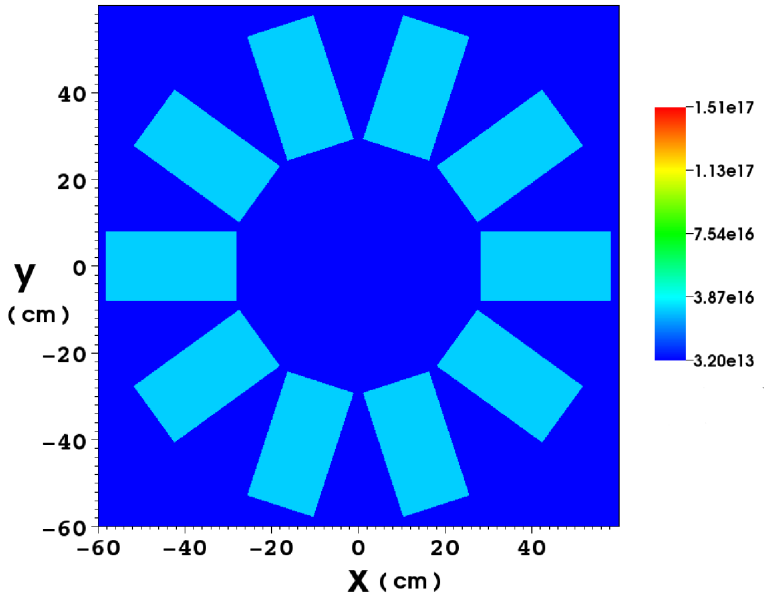

(a)

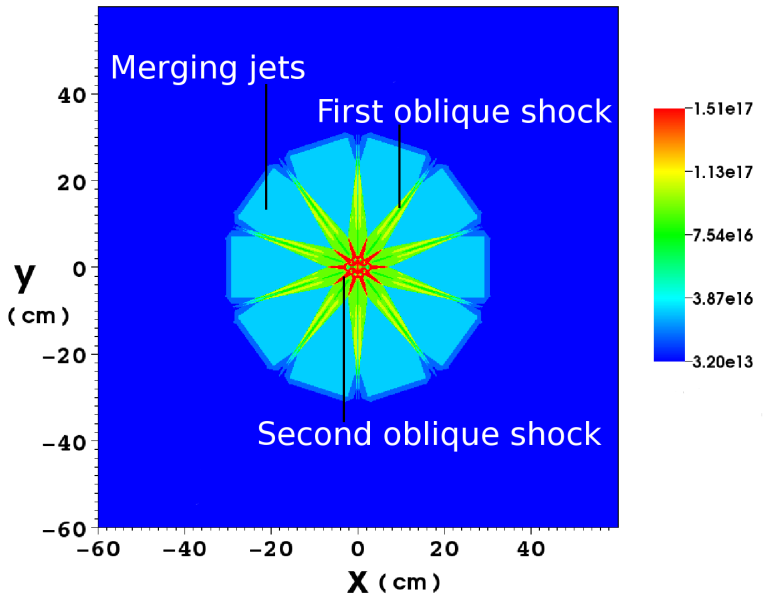

(b)

Figure 3.19: (a) Initial density of the 2D jet merger simulation and (b) density distribution showing the first and second cascades of oblique shocks. $(1/cm^2)$ (Joint Work with L. Zhang)

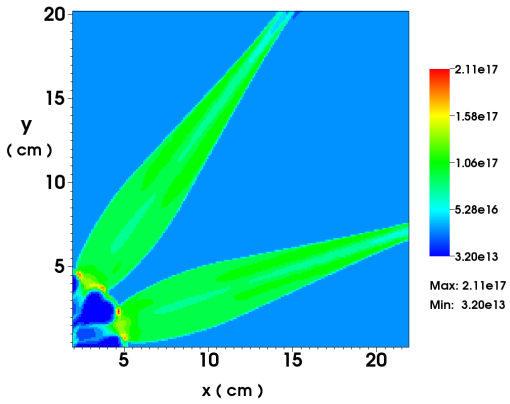

(a) Number density, $1/cm^2$

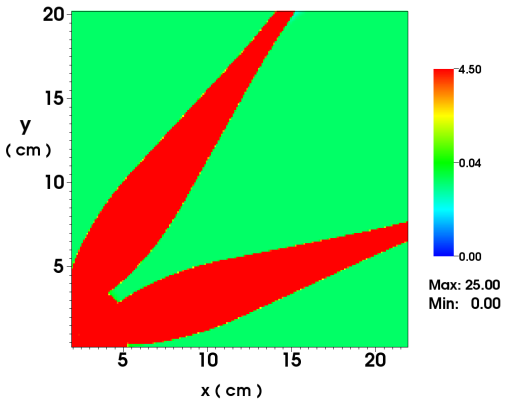

(b) Pressure, bar

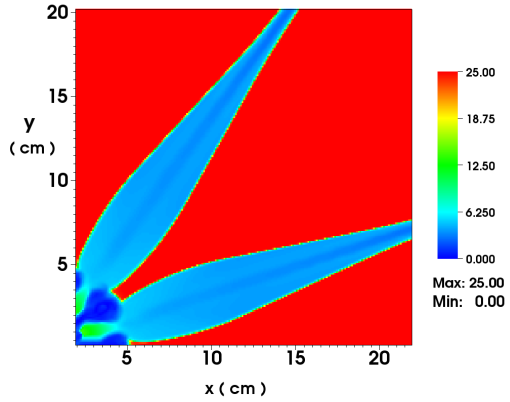

(c) Mach number

Figure 3.20: First cascade of oblique shock waves in 2D jet merger simulation. (Joint Work with L. Zhang)

	α	M_2	ρ_2/ρ_1	T_2/T_1	P_2/P_1
Theory	24.8	3.9	3.9	35	137
Simulation	23.5	4.0	3.5	35	135

Table 3.1: Comparison of simulations and theory of states in the first oblique shock wave. (Joint Work with L. Zhang)

is parallel to the mid-plane between the adjacent plasma jets. In this 2D simulation of plasma jets merger, the initial angle between two close jets is 36 degree before the first oblique shock wave and the two parts of each plasma jet, which is divided via oblique shock wave, is propagating with angle of 36 degree after the first oblique shock wave. The second oblique shock waves are produced after the first one and the wedge angle is same with the previous one. In Figure 3.21, the distribution of states of density, pressure, and Mach number after the formation of the second oblique shock are depicted and in Table 3.2, the corresponding comparison between the simulation result and the oblique shock theory are provided. In this simulation, the cascade of oblique shock waves can continue until the merged plasma jets implode in the center of simulation domain if residual vacuum gas in front of the head of plasma jets is not prevent the dynmaics of the merged plasma jets. But the next oblique shock waves is not obtained in this simulation because of the interaction between remnant gas and imploding plasma liner. Because of interaction between the residual gas in front of jets and the imploding jets, the third oblique shock waves were not resolved clearly. If we can have an idealized condition in the vacuum region, the third oblique shock waves would be obtained in this geometry condition.

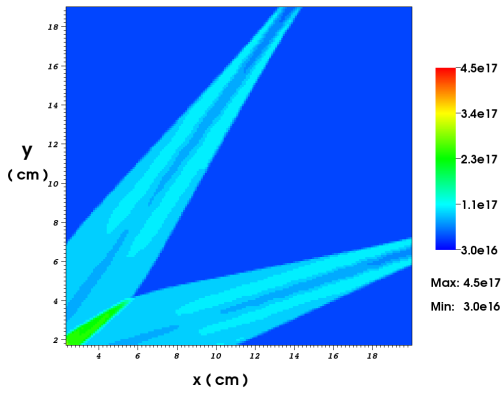

(a) Number density, $1/cm^2$

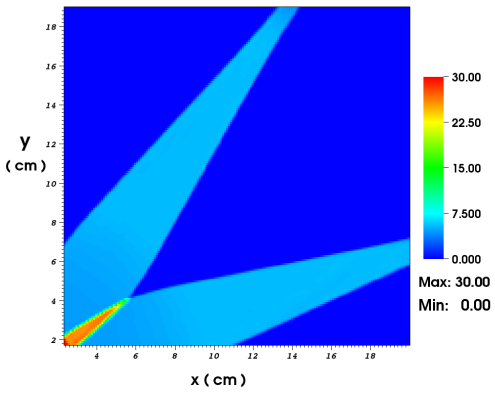

(b) Pressure, bar

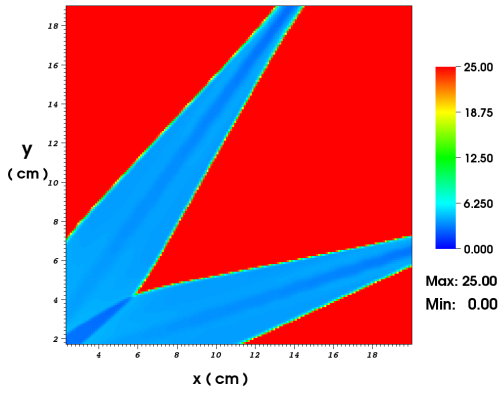

(c) Mach number

Figure 3.21: Second cascade of oblique shock waves in 2D jet merger simulation. (Joint Work with L. Zhang)

	α	M_2	ρ_2/ρ_1	T_2/T_1	P_2/P_1
Theory	33	2.3	2.4	2.3	5.6
Simulation	30	2.4	2.5	2.3	5.3

Table 3.2: Comparison of simulations and theory of states in the second oblique shock wave. (Joint Work with L. Zhang)

3.3.4 Analysis of 3D Plasma Liner

In the previous section, the comparison between the oblique shock theory and the 2D simulation of plasma jets was performed. In this work, we show that the structure and efficiency of the plasma liner is determined by the the cascade of oblique shock waves during the merger process of discrete plasma jets. If the plasma liner remains supersonic after the cascade of oblique shock waves, it can produce a central shock on a target plasma in the center.

While the precise analysis is possible in the 2D simulation of plasma jets merger, it is difficult to obtain the accurate theoretical analysis of the 3D simulation of plasma jets merger becuase of the following reasons: First, when we check the Figure 3.22, the formation of the oblique shock waves is complex comparing with the 2D case. In 2D case, the oblique shock waves are produced by the interaction between two adjacent plasma jets, but in 3D plasma jets case, these are occurring in the two and three plasma jets interaction. In the case of oblique shock wave by three plasma jets, the wedge angle is not accurate for applying the formal oblique shock theroy.

Second, single plasma jet from plasma gun is propagating around $100cm$ before the interaction with adjacent plasma jets and expanding in the domain

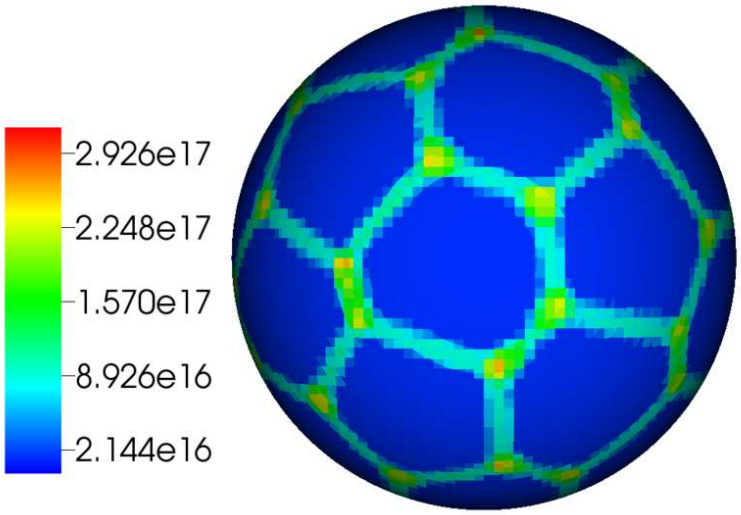

(a) Number density, $1/cm^3$

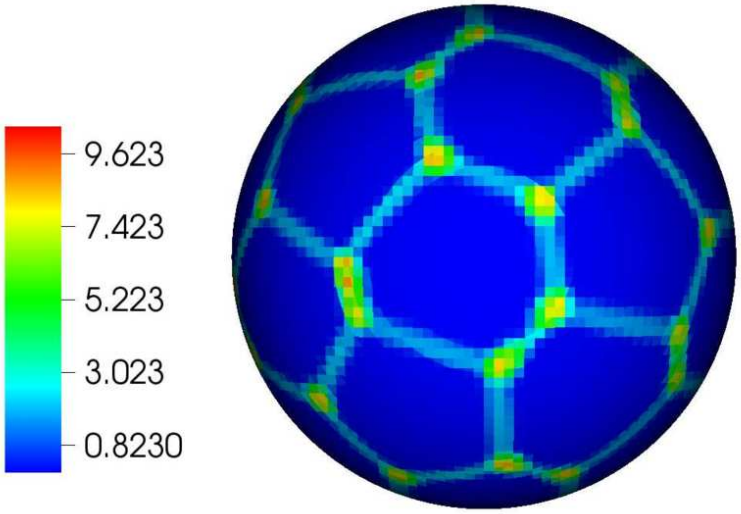

(b) Pressure, bar

Figure 3.22: Distribution of density and pressure on a 10 cm radius spherical slice of 3D liner data when t = 0.0253 ms. (Joint Work with L. Zhang)

with vacuum condition. Through this movement, the outer part of plasma jet attains a transverse directional velocity which is almost 6% of the moving velocity into the center of domain. This velocity obtained from expansion of plasma jet, can change the interaction angle between neighboring plasma jets and the distribution of transverse velocity is not uniform inside of plasma jets. Because of these effects, it is difficult to apply the oblique shock theory directly into this case. Third, the ionization level of plasma jets has changed across the oblique shock waves. In the 3D simulation of plasma jets merger, the ionization level of plasma jets has changed by the factor of 4. The formulas for oblique shock theory is based on the constant number of atoms (ideal gas) and this condition is not consistent with this 3D case.

These factors restrict the application of oblique shock theory directly to the 3D simulation of plasma jets merger and the approximate comparison with the theory is not accurate enough to understand the merger process of plasma jets. The 1D simulation of plasma liner in spherically symmetric system has performed based on the information from 3D simulation of plasma jets. By averaging the quantities of plasma jets in 3D simulation along the radial coordinate at the merging radius, the density and pressure of 1D plasma liner has been initialized and the residual vacuum condition in front of plasma liner is also taken from the 3D simulation. The evolution of Mach number in the cases of 1D plasma liner and the 3D merger of plasma jets are depicted in Figure 3.23. The initial Mach number of 3D merger of plasma jets is higher than the 1D case and this is caused by the expansion of 3D plasma jet in vacuum space shown in Figure 3.13(d). In Figure 3.23, the average Mach

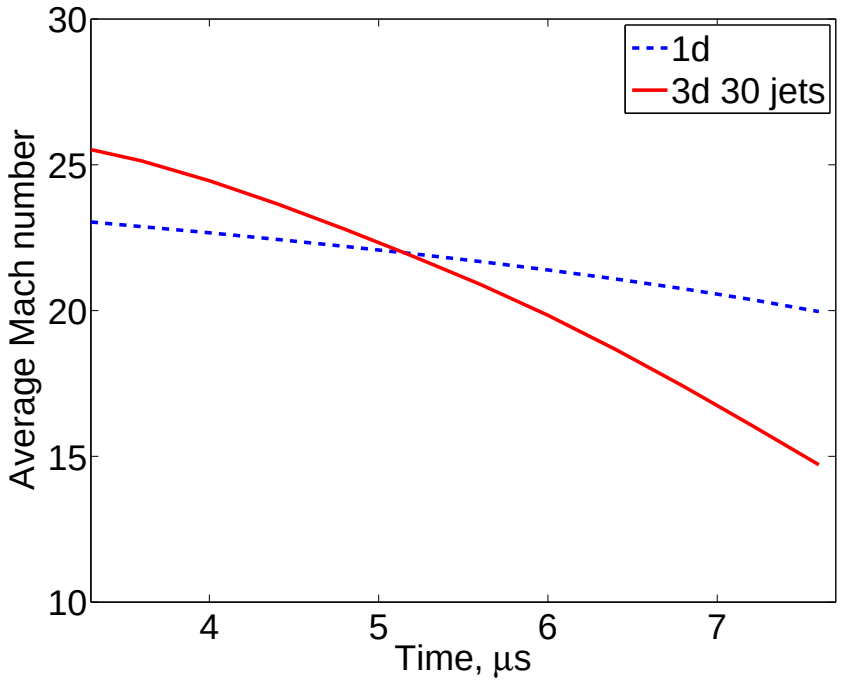

Figure 3.23: Evolution of average Mach numbers of 1D and 3D liners. (Joint Work with L. Zhang)

number of 3D merger of plasma jets is decreasing faster than the 1D case and approaching the value of 14.4 while it is 19.5 in the 1D case. Although there is a decrease of Mach number in the case of 1D plasma liner becasue of compression during implosion, the Mach number of 3D merger of plasma jets is decreasing faster because there is an additional heating by the cascade of oblique shock waves.

Three simulation results are compared and shown in Figure 3.24. Beside the 3D simulation of plasma jets merger, the two 1D simulations of plasma liners are performed. These 1D simulations are initialized based on the 3D simulation data and these 1D plasma liners have the same mass with the 3D

case. The difference between two 1D cases are the initial profile of density and the one is taken from the 3D merger of plasma jets and the other one has a sharp profile which is usually used in the previous numerical studies of 1D plasma liners. In the values of peak pressure during stagnation, the 3D simulation of plasma jets merger has produced 6.4 kbar which is 10 times smaller than the case of 1D plasma liner of same density profile as the 3D case and 50 times smaller than the case of 1D case with sharp density profile. In [8], the maximum pressures of 3D simulation of plasma jets merger and a spherically symmetric plasma liner are reported as having the same values and this contradicts our simulation result. In the vacuum region in front of the plasma liners, we apply the EOS with atomic processes to mitigate the compression effect by the plasma liners. In these simulations, we observe that an artificially increased pressure in front of plasma liner is suppressed through the energy sink by ionization process. When we applied the EOS with ionization process in the vacuum region, the peak pressure of 1D plasma liners during stagnation has increased by 30 times compared to the case of polytropic EOS in the front of plasma liner. The radiation transport was also reported for the mitigation of vacuum region in [7].

The state profile of 3D merger of plasma jets has been checked along surfaces near the potential target because the plasma liners are introduced for the compression of magnetized plasma target in the nuclear fusion experiment. On the 10 cm radius spherical slice, the profile of density and pressure of 3D plasma liner are depicted in Figure 3.22. We can check the properties about the state of the 3D plasma liner before the interaction with potential

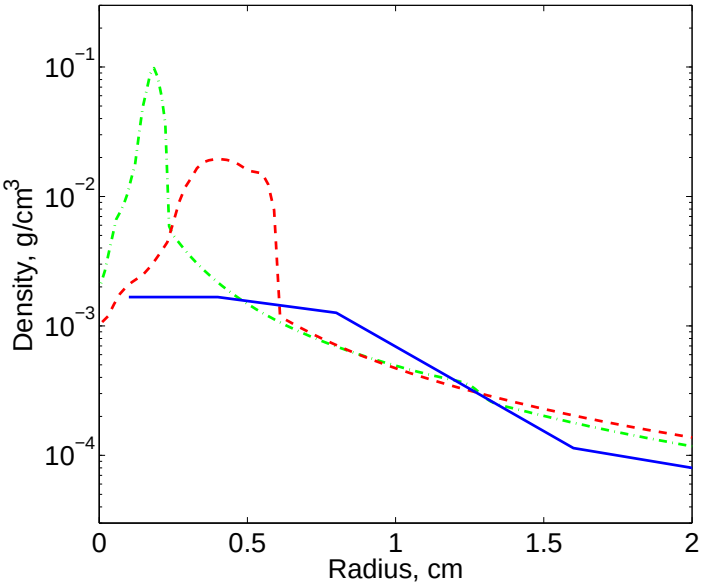

(a)

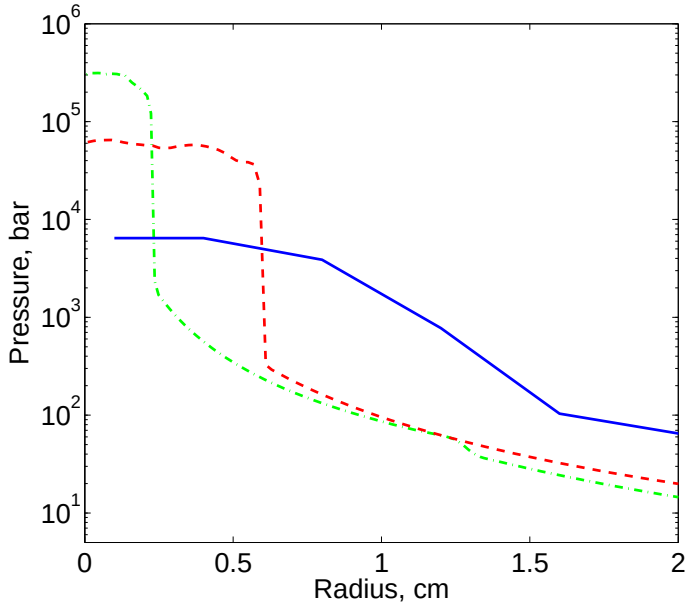

(b)

Figure 3.24: Distribution of density (a) and pressure (b) during stagnation of the 3D liner averaged in radial coordinates (solid blue line), the 1D liner initialized with sharp profile at the merging radius (green dash-dotted line) and the 1D liner initialized with same profile as the 3D liner at the merging radius (red dashed line). (Joint Work with L. Zhang)

target. In 3.22, there are variations of density and pressure of almost 10 times, which are caused by the cascade of oblique shock waves during the merger processes. Because of this non-uniformity of plasma liners, there will be a severe instability in the target during the compression by plasma liner.

In Figure 3.25, the convergence study of 3D simulation of plasma jets merger are shown. In the 3D simulation of plasma jets merger, the domain size is $(160cm)^3$ and the mesh size is $(400)^3$. The averaged Mach numbers on different mesh size has depicted in Figure 3.25. We also have performed the convergence test using the polytropic EOS model and obtained that the mesh block size of 0.4 cm is sufficient for getting accurate 3D simulation of plasma jets merger.

3.4 Two Jets Merger Simulation

3.4.1 Initialization from PLX in LANL

The PLX group at LANL has provided the experiment results about a single argon plasma jet propagation and the two obliquely merging argon plasma jets in [1, 45, 48–50]. Following these benchmark experiments, we have performed the numerical simulation work of single plasma jet moving and two plasma jets merger with consistent initial parameters from PLX group by using the FronTier code with plasma LTE EOS [10, 36].

In the simulation of two obliquely mergin plasma jets, the initialization is done with the data from the simulation of single jet propagation in the

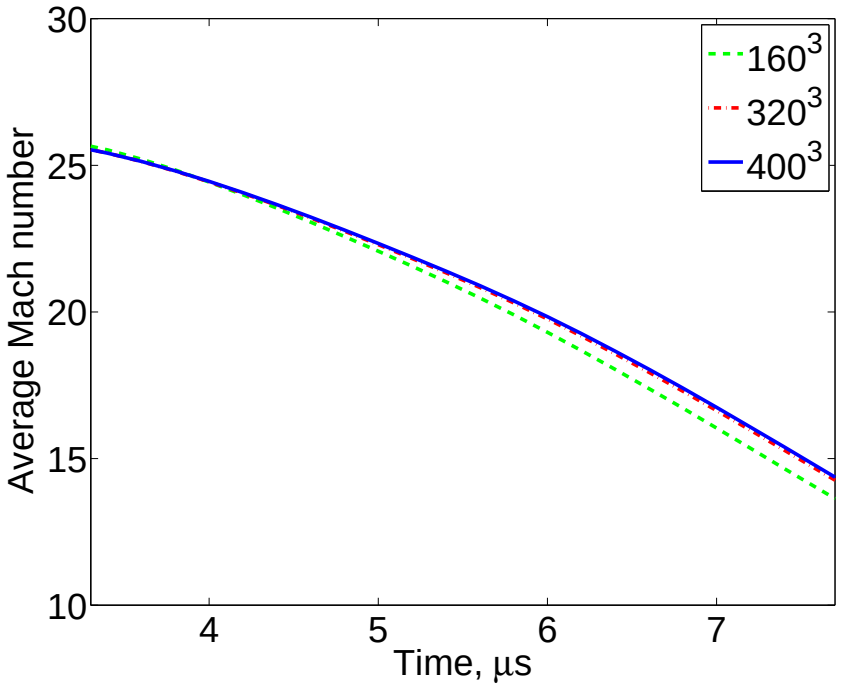

Figure 3.25: Mesh convergence studies of 3D liner formation and implosion simulation. Evolution of average Mach number using three different mesh sizes is shown. (Joint Work with L. Zhang)

2D cylindrically symmetric domain, which is a similar method to reduce the computational cost reported in [17]. The initialization of single plasma jet propagation in 2D cylindrically symmetric domain is made by using the Table II in [45]. The states of ρ = 1.327e-6 (g/cm^3), temperature T = 1.4 (eV), and velocity $V = 30$ (km/s) are initialized. This simulation was performed in a 2D cylindrically symmetric domain with open boundary conditions and the axially symmetry of plasma jet during the propagation is assumed. The mesh size in this simulation is 0.2 cm. In Figure 3.26(a), the initial density profile of single plasma jet is shown. After a time of 0.0125 ms, the density of single plasma jet is depicted in Figure 3.26(b). The simulation of 2D and 3D two obliquely merging plasma jets are initialized based on the data of single plasma jet at this time of 0.0125 ms to reduce the computational domain. In the case of single plasma jet propagation, the result from the numerical simulation is depicted in Figure 3.27 for the comparison with the experiment data in [45]. In Figure 3.27(a), we provide the average density profile of the single plasma jet, which is calculated through average along the radial direction of the plasma jet's density values. This result is consistent with the Figure 11 in [45]. We show the radial density distribution of single plasma jet in Figure 3.27(b), which is also comparable with the experiment data in [45].

In the computational domain of $(x, y) = (-20cm \sim 100cm, -35cm \sim 35cm)$ and $(x, y, z) = (-10cm \sim 90cm, -30cm \sim 30cm, -30cm \sim 30cm)$, we have performed the 2D and 3D simulation of two obliquely merging plasma jets with the mesh size of $0.4cm$ in each direction. Because of the large size of the PLX chamber, we made the subspace domain of this chamber

and the two plasma jets are merged obliquely with the degree of 24° which is coming from [49, 50]. And the positions of $(x, y) = (0.0cm, 0.0cm)$ and $(x, y, z) = (0.0cm, 0.0cm, 0.0cm)$ in 2D and 3D simulations stand for the center of the PLX chamber. In Figure 3.28(a) and 3.29(a), the initialization for two obliquely merging plasma jets are shown. A half of each plasma jet has changed abrultly because of oblique shock wave after $\sim$ 90 cm propagation, which is shown in Figure 3.28(b) and 3.29(b) for 2D and 3D simulations. The structure of two layers is shown in these figures and the same structure was also reported in [1,48–50]. In Figure 3.28(b) and 3.29(b), the distance between two layers are ($\sim 3.5cm$) which is comparable with the suppressed one-side radial length ($\sim 10cm \times \sin(12°)$) of a single plasma jet in the transverse direction to propagation way.

3.4.2 Data Post-Processing and Validation

We analyze the number density of argon atom and free electron along a line of $(x, y) = (17cm, -15cm \sim 15cm)$ in 2D case and $(x, y, z) = (17cm, 0cm, -15cm \sim 15cm)$ in 3D case for validation with the experiment observation in PLX at LANL. These simulation results are shown in Figure 3.30. The positions of $\sim 12cm$ and $\sim 18cm$ in Figure 3.30, match the two jets' center places which do not perturbed by a oblique shock wave. The difference of around one order-of-magnitude in the number density of argon atom and free electron is consistent with the result reported in [1, 48]. But this simulation result contradict the result of $\sim$ 5 times difference of electron number density shown in [49,50]. This

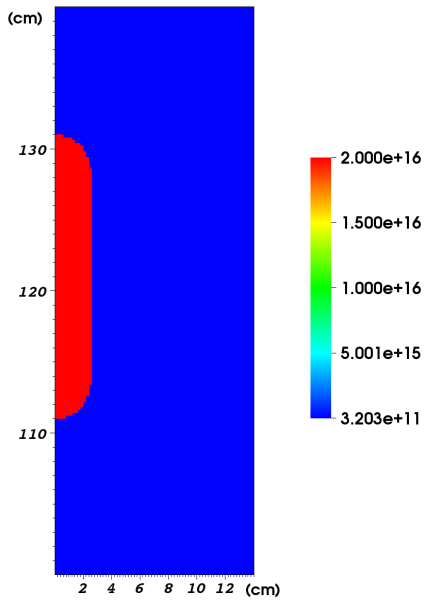

(a) t = 0.0 ms

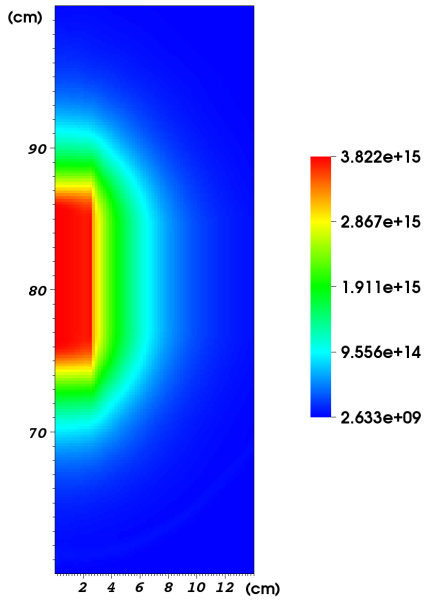

(b) t = 0.0125 ms

Figure 3.26: Density ($1/cm^3$) of the detached jet. (a) initial density; (b) density before merging radius. (Joint Work with L. Zhang)

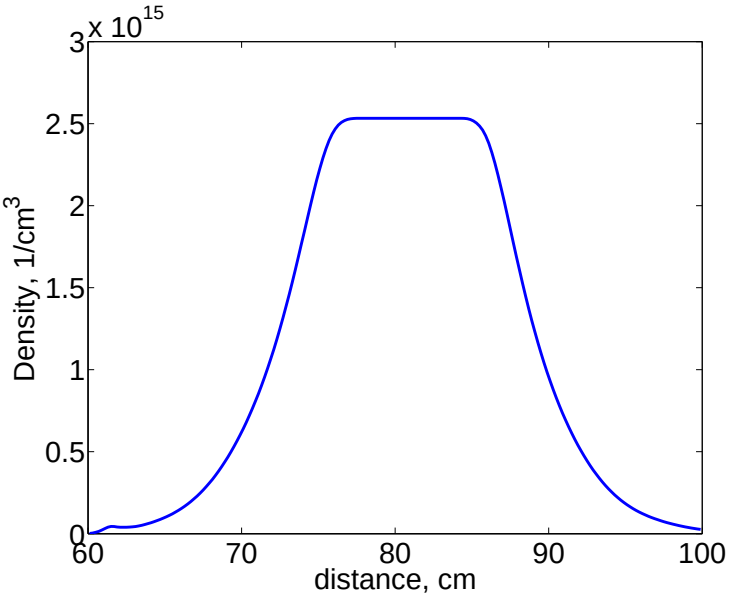

(a) t = 0.0125 ms

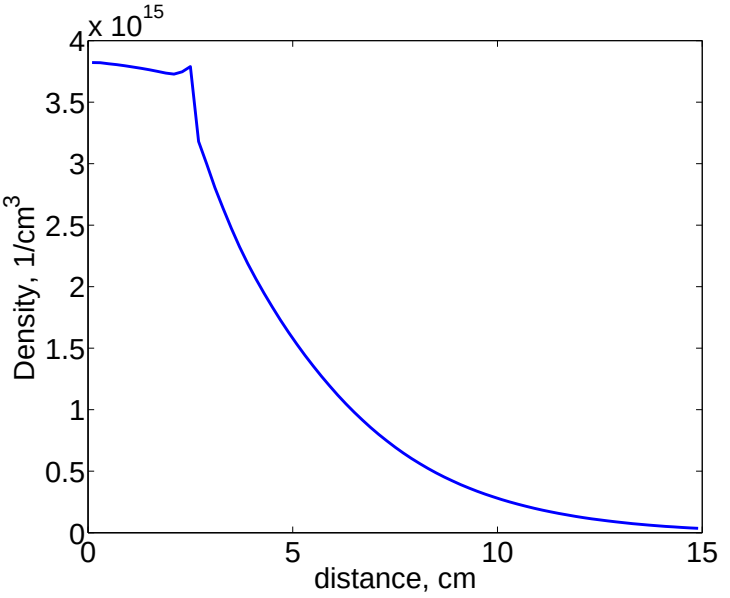

(b) t = 0.0125 ms

Figure 3.27: Density of the detached jet. (a) average number density ($1/cm^3$) over raial direction on the jet's axial direction; (b) density profile ($1/cm^3$) on the radial direction of jet. (Joint Work with L. Zhang)

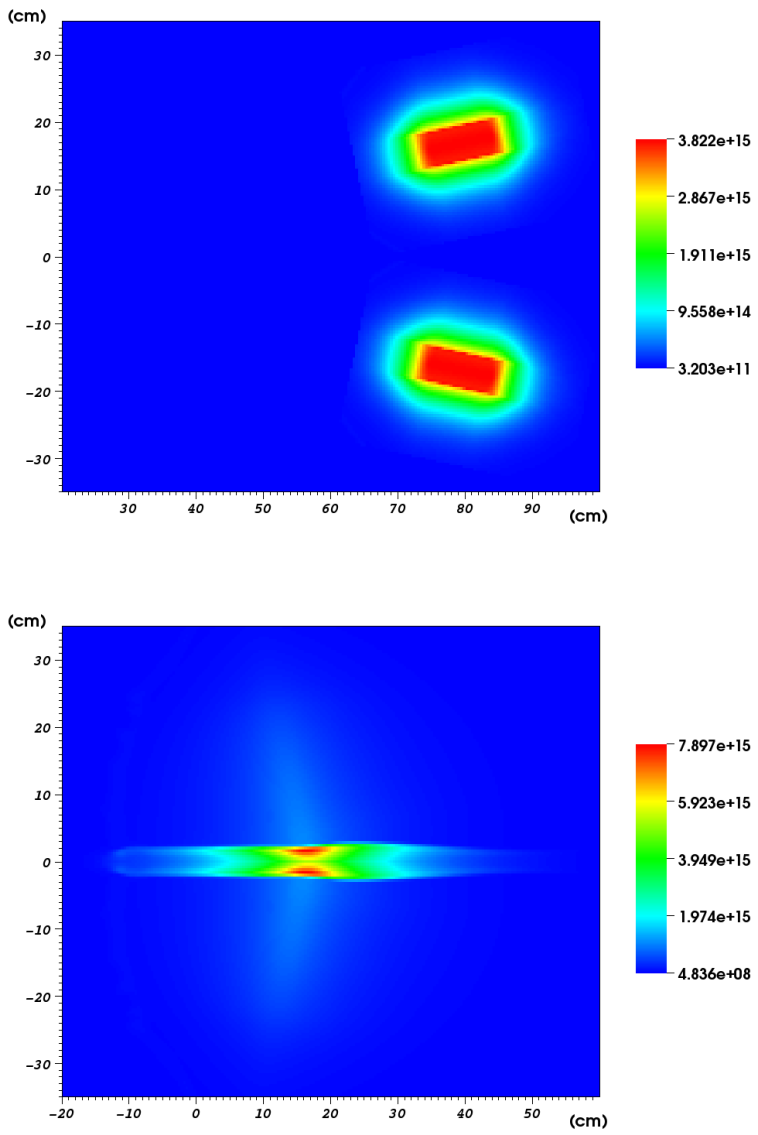

Figure 3.28: (a) 2D two jets merger simulation initial density profile ($1/cm^3$) using single jet result; (b) 2D two jets merger density profile ($1/cm^3$) after ~ 90 cm propagation from the chamber wall. (Joint Work with L. Zhang)

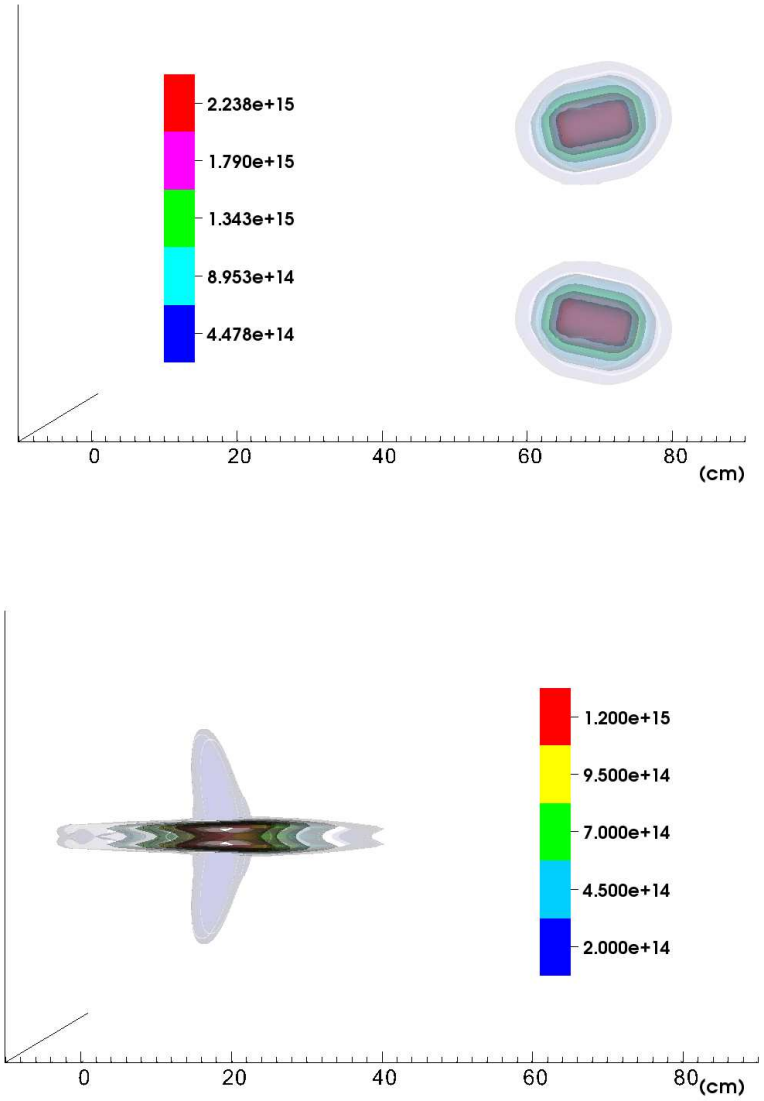

Figure 3.29: (a) 3D two jets merger simulation initial contour density profile ($1/cm^3$) using single jet result; (b) 3D two jets merger contour density profile ($1/cm^3$) after ~ 90 cm propagation from the chamber wall. (Joint Work with L. Zhang)

inconsistency can be explained through the different measurement systems for same phenomena shown in [45] and the increased temperature of plasma jet from the stored magnetic field, which are explained in the following in detail. Because of the expansion of the 3D plasma jet in the additional dimension, the density values of plasma jet in the 3D simulation is approximately 3 times lower than 2D case.

	α	M_2	ρ_2/ρ_1	T_2/T_1	P_2/P_1
Theory	14	11	7.6	1.6	12
2D	15.5	8.7	7.4	1.8	17
3D	15.5	9.3	8.8	1.8	22

Table 3.3: Comparison of results from the oblique shock wave theory and simulations of 2D and 3D. (Joint Work with L. Zhang)

The verification using the oblique shock wave theory has been performed for the other quantities of plasma jet and the result is summarized in Table 3.3. We use the local γ value of ~ 1.1 which is obtained from a γ-law fit in the plasma LTE EOS, the initial Mach number of $M_1 \sim 14$, and the wedge angle of $\delta = 12\ ^o$. Although the Mach number is the same value with [49, 50], we use the different γ value with them for analysis. As shown in Table 3.3, a reasonable result is obtained using the approximated local γ value, in spite of a fixed number assumption gas particles in the oblique shock theory. Because the dynamics of oblique shock wave is determined by the γ value, initial Mach number, and the wedge angle, which are shared by 2D and 3D simulations, the simulation results of 2D and 3D cases are very similar as shown in Table 3.3. We can explain the discrepancy between simulation results and

the oblique shock theory through the non-uniform properties of plasma jet via expansion in vacuum condition while the difference between 2D and 3D cases can be understood in the point of different expansion rate caused by additional dimension.

To justify this simulation study, the ion-ion mean free path estimates are calculated for the inside part of jet and jets merger cases. The mean free path inside of jet is evaluated as [55]

$$\lambda_i = v_{Ti}/\nu_i, \tag{3.8}$$

where the ion thermal velocity is $v_{Ti} = 9.79 \times 10^5 \mu^{-1/2} T_i^{1/2}$ cm/s, and the ion collision rate is $\nu_i = 4.80 \times 10^{-8} Z^4 \mu^{-1/2} n_i T_i^{-3/2} \ln\Lambda$, $1/s$. With the plasma jet edge's parameters ($T_i \sim 0.8$ eV, $Z \sim 1$, $n_i \sim 2.4 \times 10^{14}\, 1/cm^3$, $\ln\Lambda \sim 10$), we obtain $v_{Ti} \sim 1.83 \times 10^5$ cm/s, $\nu_i \sim 2.5 \times 10^7$ 1/s, and $\lambda_i \sim 5.5 \times 10^{-3}$ cm, which justify the single plasma jet simulation study. For the inter-jet case, the slowing down of a penetrating ion is estimated as [55]

$$\frac{dv_\alpha}{dt} = -\nu_s^{\alpha\backslash\beta} v_\alpha \tag{3.9}$$

where $\nu_s^{\alpha\backslash\beta} = (1 + m_\alpha/m_\beta)\psi(x^{\alpha\backslash\beta})\nu_0^{\alpha\backslash\beta}$, $\nu_0^{\alpha\backslash\beta} = 4\pi n_\beta e_\alpha^2 e_\beta^2 \lambda_{\alpha\beta}/m_\alpha^2 v_\alpha^3$, $x^{\alpha\backslash\beta} = m_\beta v_\alpha^2/2kT_\beta$, and $\psi(x) = \frac{2}{\sqrt{\pi}} \int_0^x t^{1/2} e^{-t} dt$. With the plasma jet edge's states and $\lambda_{\alpha\beta} \sim 10$, we obtain that the ion's penetrating velocity ($v_\alpha^{initial} \sim 1.2 \times 10^6\ cm/s$) is slowed down to thermal velocity after moving of around 0.7cm. Because of highly collisional electrons and electrostatic interaction, the depth

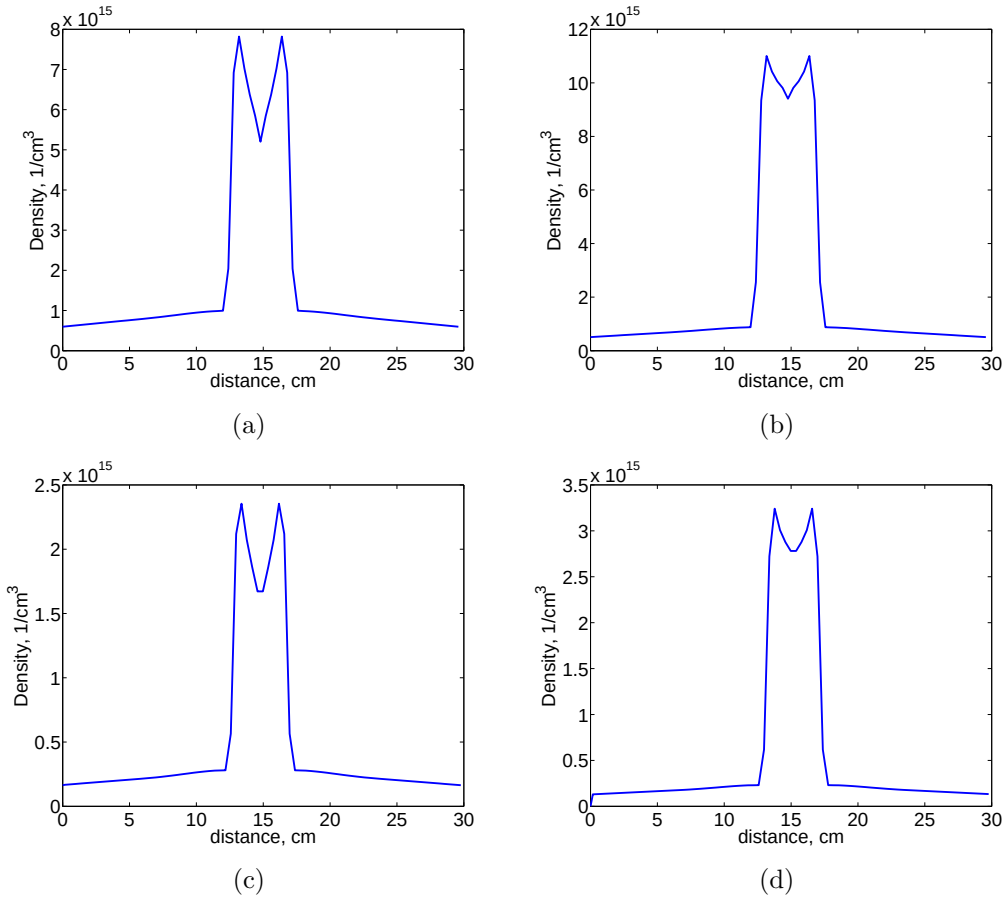

Figure 3.30: 2D two jets merger transverse argon atom density(a) and electron density(b) profile; 3D two jets merger transverse argon atom density(c) and electron density(d) profile at the position of ~ 90 cm from the chamber wall. (Joint Work with L. Zhang)

of ion penetration into the other plasma jet will be decreased further, which justify the single fluid model study for two jets merger process.

The stored magnetic field enegy is explained in [45]. Here the initial stored magnetic field energy ($B^2/2\mu_0$ in MKS unit system) is reported around ~ 36 (unit system of (g,cm,ms)) in the plasma gun bore (magnetic field ~ 3 T). The internal energy of plasma jet (number density $\sim 2 \times 10^{16}$) depending

on the temperature is shown in the Figure 3.31(a). So the plasma jet with (number density $\sim 2 \times 10^{16}$ and T $\sim$ 1.4 eV) has a $\sim$ 30 times smaller internal energy comparing with the stored magnetic field energy. Because the accurate conversion process of stored magnetic field energy into other energy forms are not resolved, our simulation work is limited. But, if a non-negligable portion of the magnetic field energy is converted into the internal energy of plasma jet, the Mach number of the plasma jet will be changed a lot because of the sensitivity of Mach number on internal energy shown in the Figure 3.31(b).

In [49, 50], the experiment result of two obliquely merging plasma jets is reported. In this observation, the oblique shock wave angle ($\alpha \sim 17^o$) and the increased interferometer $\Delta\phi$ measurement of the merged jet ($\sim$ 4 times higher value for the merged jet) are the part of the main result. Although the reported initial Mach number of the plasma jet is ($\sim$ 14) in [45, 49], when we compare these reported values of α and $\Delta\phi$ with the simple calculation result which are shown in Figure 3.31(c) and Figure 3.31(d), we conjecture that the Mach number of single plasma jet could be decreased when the merger of two plasma jets is occurring.

Initial Temperature	M_1	ρ_2/ρ_1
1.4 eV	~ 14	~ 8.5
2.0 eV	~ 11	~ 7.5
2.5 eV	~ 9.5	~ 6.5

Table 3.4: 2D simulation result of two jets merger with different initial temperature at $\sim$ 100 cm from the chamber wall.

The 2D simulation work of the merger of two plasma jets was done to study

the effect of dissipation of a stored magnetic field energy inside the plasma jet. The initial state of single plasma jet (number density $\sim 2 \times 10^{16}$ and plasma jet velocity $\sim 30\ km/s$) is consistent with the observation in [45]. The only difference is the variation of plasma jet's initial temperature and the higher initial temperature tried to mimic the magnetic field energy. When the two plasma jets are passing the position of ($\sim 100\ cm$ from the chamber wall), the Mach number of jets and density ratio across the oblique shock wave are shown in the Table 3.4. Clearly the tendency of the Mach number and density ratio across an oblique shock wave is consistent with the previous calculation result in Figure 3.31(b) and Figure 3.31(d).

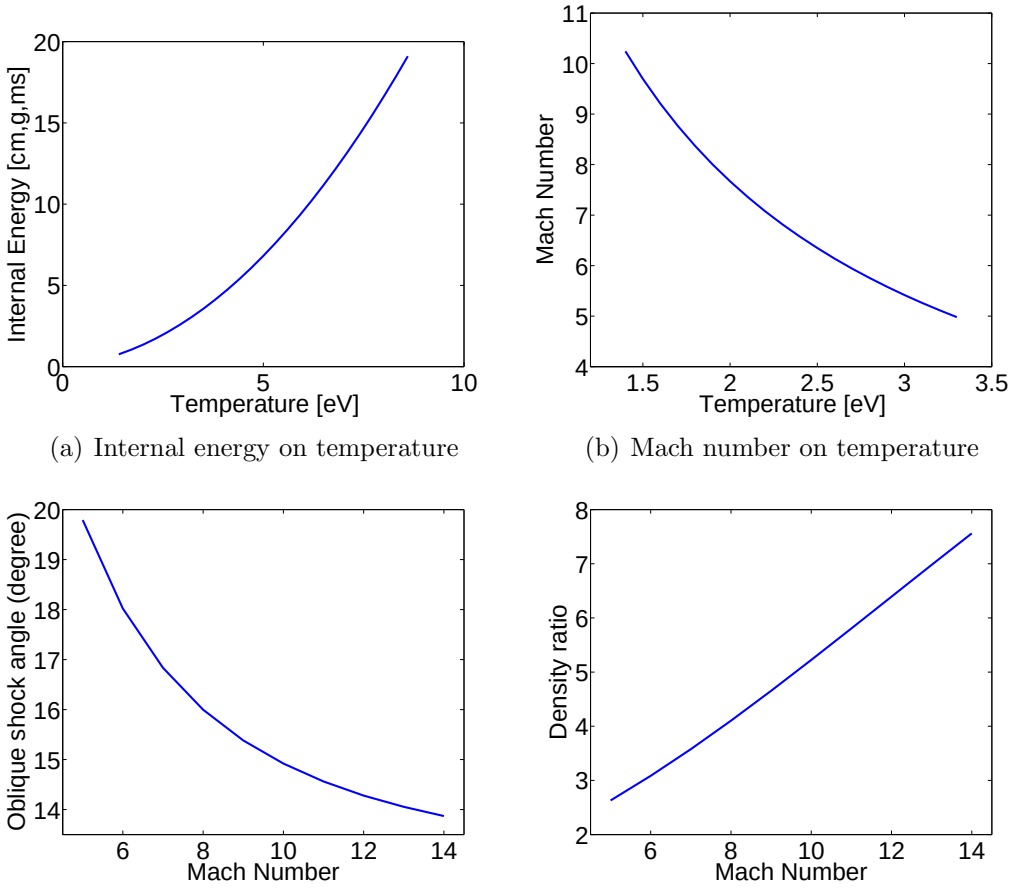

(a) Internal energy on temperature

(b) Mach number on temperature

(c) Oblique shock angle on Mach number

(d) Density ratio on Mach number

Figure 3.31: The properties of plasma jet depending on varying temperature and Mach number.

Chapter 4

Pellet Ablation in Thermonuclear Fusion Devices

4.1 Introduction

As details of transonic regimes of the pellet ablation flow are strongly dependent on atomic physics processes in the ablation cloud, the quality of numerical equation of state models describing partially ionized plasmas is of significant importance. While probabilities of multiply ionized states in high-Z materials in the local thermodynamic equilibrium is accurately described by coupled system of Saha equations [11], the direct use of these equations in time-dependent hydrodynamic simulations is prohibitively computationally intensive. In our previous works [10, 17], we have developed a numerical EOS model for argon based on the Zel′dovich approximation of average ionization [11]. The average ionization model (AIM) relates the average ionization level $\overline{m}$ with the

thermodynamic states as $\overline{m} = \frac{AT^{3/2}}{n} \exp -\frac{\bar{I}}{kT}$ and computes the pressure as $P = (1 + \overline{m})\rho RT$.

We compare simulations of high-Z gases with molecular deuterium described in [9,23,24]. The equation of state model for deuterium that accounts for dissociation and ionization uses the exact system of Saha equations. We also compare our results with simulations obtained using the polytropic EOS model that defines the gas pressure as $P = (\gamma - 1)\rho e$, where γ is the ratio of specific heats.

The electron heat flux model is identical to that of the previous works [9,23, 24,59] except the modification of the Coulomb logarithm and the dimensionless opacity for high-Z atoms. The modified Coulomb logarithm is:

$$\ln \Lambda = \frac{\overline{m}}{Z} \ln \Lambda_{ef} + \frac{(1 - \overline{m})}{Z} \ln \Lambda_{eb}$$

in which Z=atomic number, $\Lambda_{ef} = 0.2E/\hbar\omega_{pe}$, $\omega_{pe} = (4\pi n_e e^2/m_e)^{1/2}$, $\Lambda_{eb} = E/I_*\sqrt{e/2}$, $E \approx 2T_{e\infty}$(plasma electron temperature), n_e=plasma electron density, and I_* is the mean excitation energy (for example, $I_*^H = 19.2$ eV, $I_*^{Ne} = 137$ eV, and $I_*^{Ar} = 188$ eV from [60]). The changed dimensionless opacity in the spherically symmetric approximation is $u = \tau/\tau_{eff}$, where

$$\tau(r) = Z \int_r^\infty n(r')dr', \qquad \tau_{eff} = \tau_\infty \sqrt{\tfrac{2}{1+Z}}, \qquad \tau_\infty = \tfrac{T_{e\infty}^2}{8\pi e^4 \ln \Lambda}.$$

The pellet surface ablation model is identical to that of [9] with the exception of some technical improvements, namely the numerical treatment of high

gradients of physics quantities near the pellet surface.

In this chapter, all simulations of pellet injection were performed in 1D spherically symmetric domain with a mesh size of 0.005 cm, the phase transition boundary condition on pellet surface, and the open boundary at outer region.

4.2 1D Studies of Ablation of Deuterium Pellets

We start with the simulation of a deuterium pellet using parameters of [9], namely the pellet radius of $r_p = 0.2cm$, the plasma electron temperature of $T_{e\infty} = 2keV$, and the plasma electron density of $n_{e\infty} = 10^{14}cm^{-3}$. Simulations with the polytropic EOS demonstrate a transonic ablation flow that starts as subsonic near the pellet surface and changes to supersonic due to the electron heat flux (Figure 4.1). When the deuterium plasma EOS is used (Figure 4.1), the ablation flow is affected by energy sinks due to the dissociation and ionization. The dissociation processes slow down the increase of the Mach number near the pellet surface. The flow accelerates then to supersonic velocities before the majority ionization processes occur. The ionization energy causes the shock wave and the drop of the Mach number below unity. The flow then accelerates again and reached the supersonic state the second time (double transonic pellet ablation regime). The temperature T^* and pressure P^* of the ablation cloud at the sonic radius r^* are shown in Table 4.1. The ablation

rate using polytropic EOS in Table 4.1 is consistent with the value of 133 g/s predicted by the theoretical transonic flow model of [29]. The ablation rate is reduced by approximately 10.7% when the atomic processes are included in the EOS.

	r* (cm)	T* (eV)	P* (bar)	Ablation rate (g/s)
Polytropic EOS ($\gamma = 7/5$)	0.518	3.21	29.25	132.6
Plasma EOS	0.474	1.04	25.54	118.4

Table 4.1: The ablated cloud states of deuterium pellet at the first sonic radius (r*) for the cases with polytropic EOS and plasma EOS.

4.3 Effect of Ionization on the Ablation of Argon and Neon Pellets

In the pellet ablation simulation of neon and argon, the states of the ablation cloud at sonic radius are shown in the table 4.2 and 4.3 and the normalized quantities based on them are provided in Figures 4.2 and 4.3. For simulations that neglect ionization using the polytropic EOS, the ablation rates in Tables 4.2 and 4.3 are in reasonably good agreement to the theoretical predictions of 109 g/s for neon and 103 g/s for argon using the transonic flow model [29]. The ablation flow of the neon pellet exhibits the double transonic regime similar to the deuterium case. Slowly increasing ionization potentials of the neon atom corresponding to the ionization levels from 1 to 8 irregularly reduce the ablation flow acceleration and cause oscillations on the Mach number plot

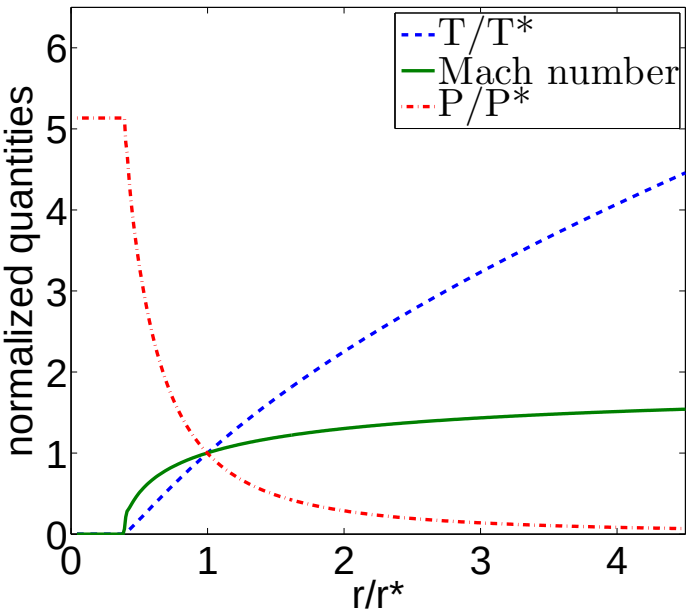

(a) Polytropic EOS

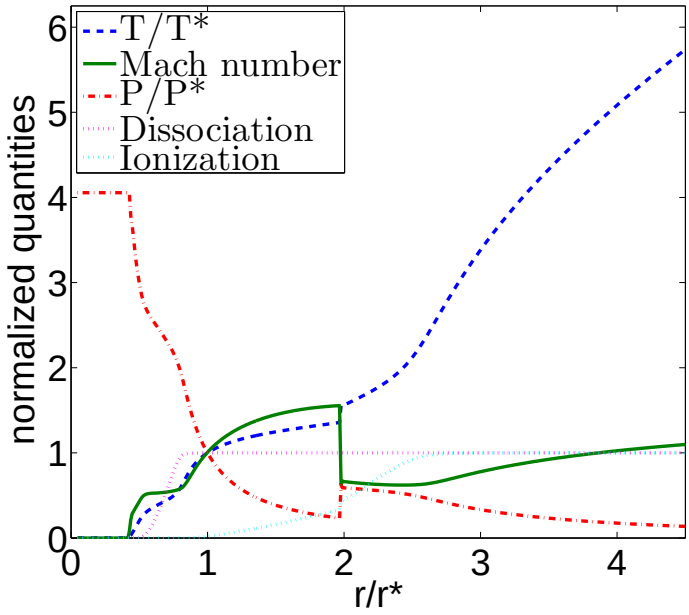

(b) Plasma EOS

Figure 4.1: Normalized ablated cloud profiles of deuterium pellet in 1D spherically symmetric model of ablation (a) without atomic processes (polytropic EOS), and (b) with atomic processes (plasma EOS).

in Figure 4.2(b). Despite these energy sinks, the flow accelerated above the sonic point. Then the large increase of the ionization energy associated with stripping off the 9th and 10th electrons drop the Mach number below unity and cause the shock wave. Then the flow again reaches the supersonic state.

The ablation flow regime is more complex for the argon pellets (Figure 4.3(b)). The ionization energy of the argon atom slowly increases with the increase of the ionization level from 1 to 16, with the exception of a bigger change of the ionization potential between levels 8 and 9 (see Figure 2.5). Nevertheless, the Mach number twice drops below unity before the average ionization reaches level 6 (see Figure 4.4 that shows details of the Mach number and the average ionization close to the pellet surface). This is caused by the combination of the increasing ionization energy with statistical weights that rapidly increase for the ionization level 3 and 6 (see Figure 4.4), causing the weak shock waves in the ablation flow. Then the flow slowly and steadily accelerates under constant energy removal by ionization. When the ionization level reaches 16, the rapid increase of the ionization potential between levels 16 and 17 causes the third shock wave. Then the flow of fully ionized argon accelerates again above the sonic point.

A large reduction of temperature in the neon and argon pellet simulations with real gas EOS compared to the polytropic gas simulations can be understood via consecutive ionization energy losses. For the argon pellet, there is one order of magnitude difference of temperature at the first sonic radius (table 4.3) and this difference is consistently observed along the ablation cloud, as shown in the Figure 4.5. The reductions of the ablation rates for the neon

and argon pellets by atomic processes, $\sim 15.6\%$ and $\sim 25.3\%$ respectively, is significantly larger compared to the case of deuterium pellets. The reason for this is well understood in terms of ionization energy losses.

	r* (cm)	T* (eV)	P* (bar)	$\overline{m}$*	Ablation rate (g/s)
Polytropic EOS ($\gamma = 5/3$)	0.603	30.15	22.96	-	112.9
Plasma EOS	0.603	4.84	16.37	1.99	95.3

Table 4.2: The ablated cloud states of neon pellet at the first sonic radius (r*) for the cases with polytropic EOS and plasma EOS.

	r* (cm)	T* (eV)	P* (bar)	$\overline{m}$*	Ablation rate (g/s)
Polytropic EOS ($\gamma = 5/3$)	0.588	61.82	22.62	-	103.6
Plasma EOS	0.415	4.46	20.04	2.49	77.4

Table 4.3: The ablated cloud states of argon pellet at the first sonic radius (r*) for the cases with polytropic EOS and plasma EOS.

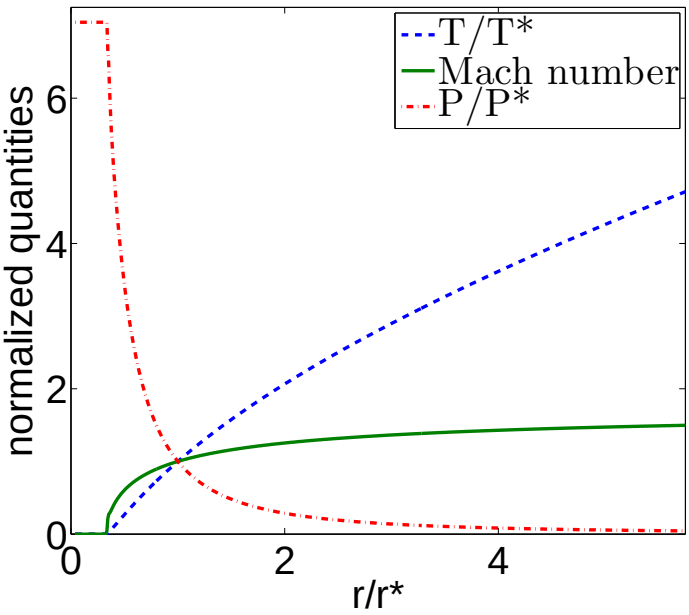

(a) Polytropic EOS

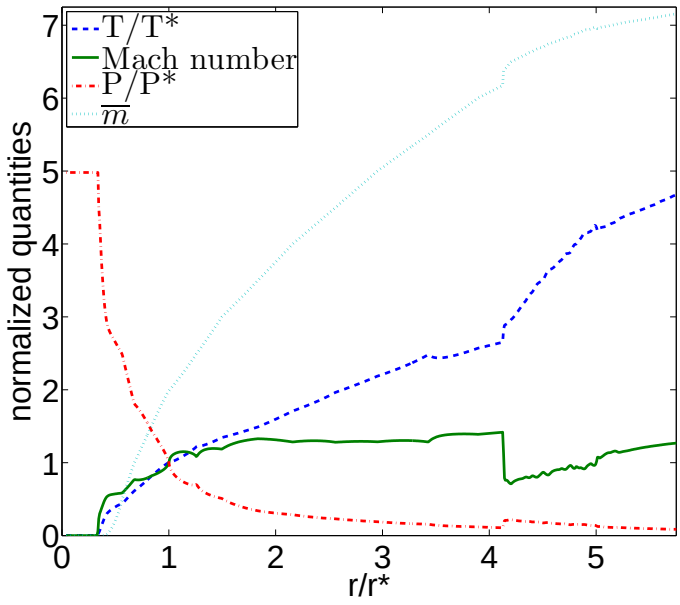

(b) Plasma EOS

Figure 4.2: Normalized ablated cloud profiles of neon pellet in 1D spherically symmetric model of ablation (a) without atomic processes (polytropic EOS), and (b) with atomic processes (plasma EOS).

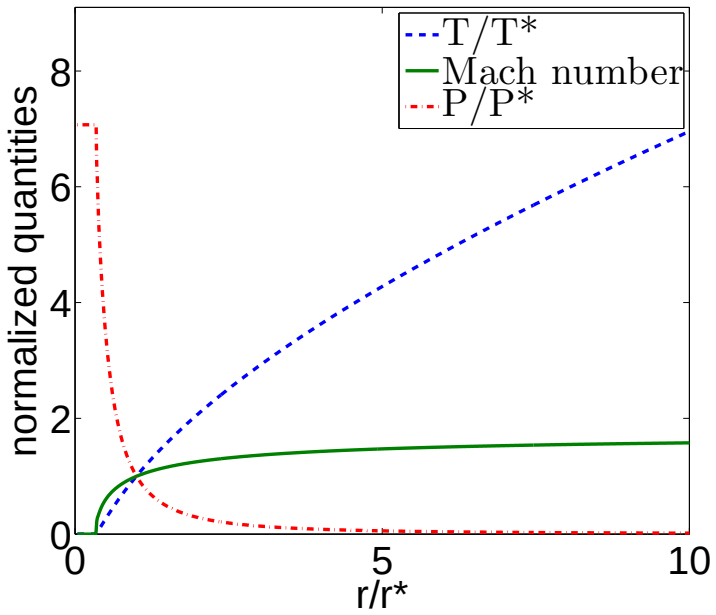

(a) Polytropic EOS

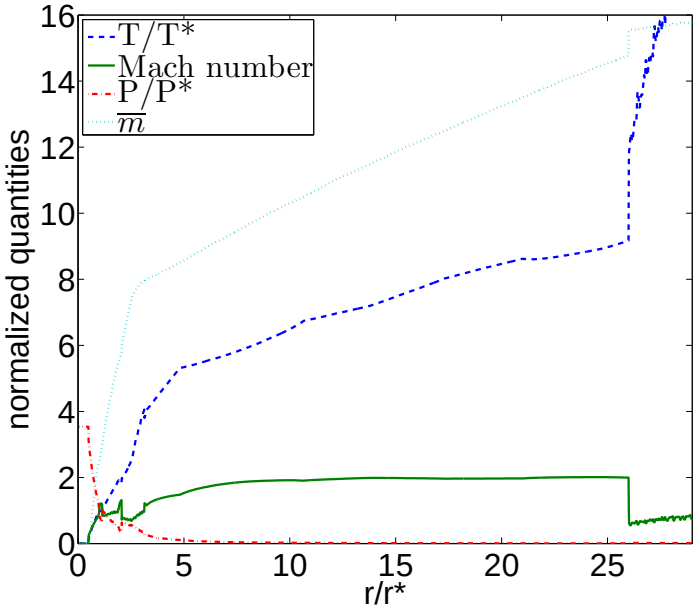

(b) Plasma EOS

Figure 4.3: Normalized ablated cloud profiles of argon pellet in 1D spherically symmetric model of ablation (a) without atomic processes (polytropic EOS), and (b) with atomic processes (plasma EOS).

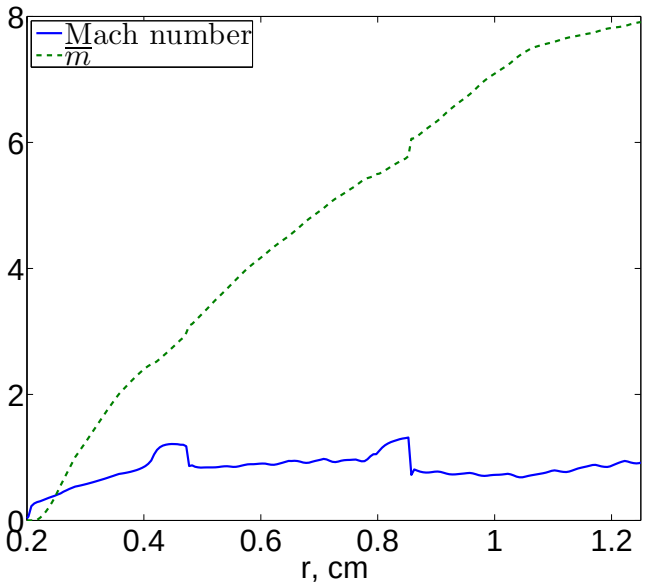

(a) Ablation flow of argon pellet

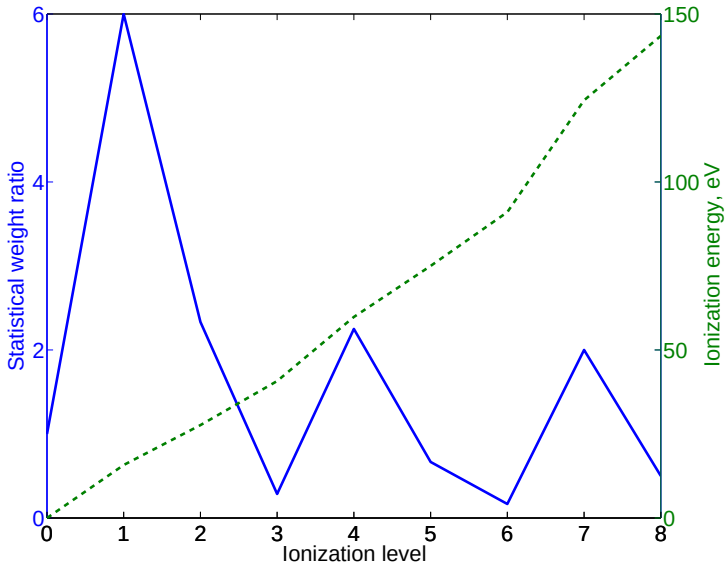

(b) Atomic property of argon

Figure 4.4: The local property of argon pellet's ablation flow near the pellet surface (a) and the corresponding atomic property of argon (b).

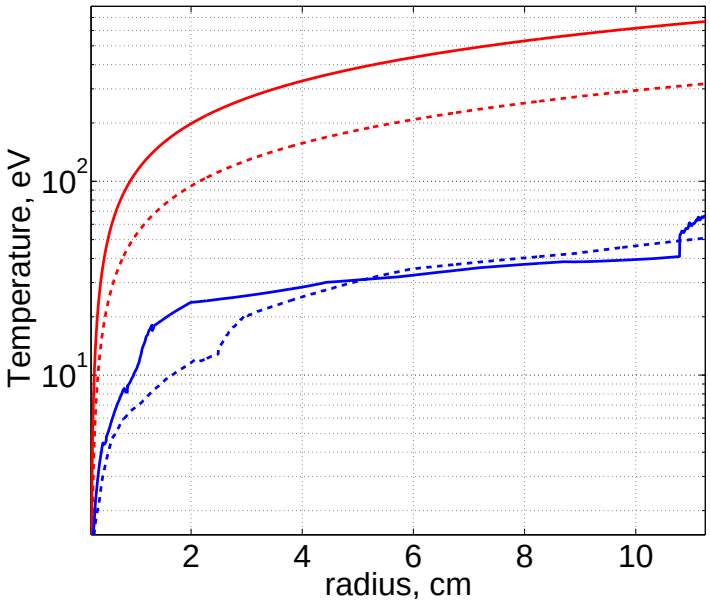

Figure 4.5: The comparison of ablated gas temperature of neon pellet (dashed line) and argon pellet (solid line) with polytropic EOS (red line) and plasma EOS (blue line).

Chapter 5

Conclusion and Future Directions

5.1 Modeling of Atomic Physics Processes in Equation-of-State

The EOS models with atomic processes of dissociation and ionization has been developed for the application in high energy density physics. [9, 10] These EOS models are applied into the simulation of pellet injection in Tokamak and PJMIF and provide a reasonable explanation about the internal structure inside of plasma flow.

The numerical EOS for high-Z atoms has developed based on the average ionization model in [11] with LTE condition. The coupled system of Saha equations has reduced into the single nonlinear equation under continuum assumption of discrete values and it has become possible in hydrodyanmic

simulation to calculate the average ionizatioin level. This model produces reasonable values comparing to the average ionization value from the system of nonlinear equations. To increase the accuracy of this EOS model in the low temperature region, the continuum value of statistical weight was used and we obtain more precise result when the average ionization is less than 1. There are other advantages of this average ionization model beside the reduction of computation cost, e.g. it can be applied into the mixture of various atoms for multispecies flow. We are working on the developement of numerical EOS for other atoms and mixture of atoms and the result will be reported in the forthcoming paper.

5.2 Plasma Jets Driven Magneto-Inertial Fusion

The concept of PJMIF was proposed in [13] as a method for inertial nuclear fusion to solve the standoff problem and the corresponding experiments were performed by PLX team in LANL reported in [45,48,49]. In [6–8,14,46,47], the theoretical and numerical studies of PJMIF are reported about the properties of plasma liners and the merging process of discrete plasma jets. But, the atomic processes such as ionization and the internal structure of the plasma jets are not resolved fully in these previous works. In this work, we apply the EOS model with atomic processes in the simulations of plasma liners. The 1D simulations of plasma liners in a spherically symmetric domain are done

to quantify the effect of the atomic processes during the implosion of plasma liner. And 2D and 3D simulations of plasma jets merger are made to resolve the internal structure of plasma jets during the merging process because this cannot be captured in the 1D simulation case.

In 1D simulations of plasma liners, we have studied the effect of atomic processes on the implosion of argon plasma liner in spherically symmetric computation domain. The FronTier code with front-tracking method was used in this numerical work and this code was mainly developed to resolve accurately material interfaces or multiphase systems with discontinuity in solutions or material properties. The verification of FronTier code has performed using the Noh problem in 1D spherically symmetric domain, and good agreement with theory and second order of convergence has obtained.

For the initialization of 1D simulations of an argon plasma liner, we use the parameters from PLX in LANL. The initial position of plasma liner is at the merging radius of 33 cm for the comparison with [7]. The Mach number of the plasma liner has increased because of the effect of ionization energy sink resolved by plasma EOS during the propagation of plasma liner. In the head part of the plasma liner, the average ionization level has increased into 7.2 and this has led the increase of density and pressure. The dynamics of plasma liner with plasma EOS model has changed significantly comparing with the case with the ideal EOS model. By including the energy sink through ionization, the stagnation pressure of 930 bar is obtained in the case of PLX1 and PLX2 from [7]. This peak stagnation pressures in our simulation work are approximately three order of magnitude smaller than the case in [7], which contained the

effect of radiational transport without ionization process. The peak stagnation pressure from the HELIOS code with the PROTACEOS non-LTE EOS in [7] is comparable with our result from the FronTier code with LTE plasma EOS. Additionally, the times of the target deconfinement and stagnation are not changed when we include the atomic processes. The overall increase of efficiency of argon plasma liner with plasma EOS is an approximately doubling of the Mach number and the stagnation pressure comparing the case with ideal EOS.

The 3D simulations of plasma jets merger were performed by using the FronTier code to investigate the internal sturcture of plasma liner produced from the merger of 30 argon plasma jets with the consistent parameters of PLX in LANL. To reduce the computational cost, 2D simulation of single plasma jet propagation from plasma gun in cylindrically symmetric domain was made and the result has embeded in the optimized 3D computational domain. In this simulation, we also applied the plasma EOS for argon which can resolve the ionization effect during the merger process.

From 3D simulations, a cascade of oblique shock waves are resolved numerically in the process of plasma jets merger. These oblique shock waves during the merger process lead to an increase of temperature, a the reduction of the Mach number, and the self-collapse pressure in the plasma liner. For the verification of the FronTier code with the oblique shock theory, we also perform the 2D simulation of plasma jets merger for the clear comparison. In this 2D simulation, a good result was obtained and the states after a cascade of oblique shock waves are consistent well with values from the oblique shock

theory. The 3D simulation of a plasma jet merger is complicated to apply the oblique shock theory directly because of the three plasma jets interaction, the plasma jets expansion in vacuum condition, and the variation of atom numbers because of ionization process. So, we analyze this 3D case by using the comparison with the 1D simulation performed in spherical symmetric domain. We initialize two 1D simulations with a sharp density profile and a density profile extracted from radial average value of 3D simulation result at the merging radius. The peak self-implosion pressures are 6.4 kbar in 3D simulation case, 64 kbar in 1D simulation with density profile from 3D simulation result, and 320 kbar in 1D simulation with a sharp density profile in the mergin radius. This difference can be explained via the internal structure of the 3D plasma liner, which caused by a cascade of oblique shock waves and resolved only through the 3D simulation. In [8], the maximum pressure values from the uniform plasma liner and the plasma liner from descrete plasma jets are approximately same and this is contradiction with our result. Convergence studies using different mesh sizes were performed, and the convergence of the Mach number was obtained. The dyanamics of plasma jet mergers can be varied depending on the number of plasma jets. If we put more plasma jets than 30 jets, the strength of the oblique shock waves will be decreased and the merging radius of plasma jets will be increased. In this 3D simulation work, the number of plasma jets is provided from the PLX in LANL and we did not consider the optimization for plasma liners.

The state profile of 3D plasma liners also was investigated for the interaction between the plasma liner and the potential plasma target in the inertial

nuclear fusion. In the values of pressure and density, there is a large variation of factor of 10 on the leading edge of the plasma liner along spherical surfaces with radius of 10cm. This property of plasma liner as a compressor of plasma target for nuclear fusion leads a possibility of severe instability during the interaction. The 3D numerical study of the interaction between the plasma liner and plasma target using the FronTier code is in progress and will be reported in a following paper. The main advantage of FronTier code is a front-tracking method which can handle the interfaces between different materials and this method matches this interaction simulation perfectly.

5.3 Pellet Ablation in Thermonuclear Fusion Devices

The simulations of high-Z pellet injection in a Tokamak, the numerical EOS based on AIM is improved by including the statistical weight of bounded electrons and more realistic ionization energy profile. The physical properties such as multi-transonic flow and ablation rate reduction related to atomic processes in 1D spherical symmetric case have been observed and compared with [29]. Base on these result, we are planning to make a 2.5-dimensional MHD simulation of high-Z pellet because the funnel phenomena [9] and rotation [24] of pellet ablation cloud can be resolved only through this simulation, including the changed ablation rate.

Bibliography

[1] S. C. Hsu et al., Summary of Plasma Liner Experiment (PLX) Research Results, *54th Annual Meeting of the APS-DPP*, 2012.

[2] See http://www.iter.org.

[3] J. Glimm, J. Grove, X. L. Li, K. L. Shyue, Q. Zhang., and Y. Zeng, Three dimensional front tracking, *SIAM J. Sci. Comput.*, **19**, 703-727, 1998.

[4] http://en.wikipedia.org/wiki/MUSCL_scheme.

[5] See http://cococubed.asu.edu/research_pages/noh.shtml.

[6] R. Samulyak, P. Parks, and L. Wu, Spherically symmetric simulation of plasma liner driven magnetoinertial fusion, *Phys. Plasmas*, **17**, 092702, 2010.

[7] T. J. Awe, C. S. Adams, J. S. Davis, D. S. Hanna, and S. C. Hsu, One-dimensional radiation-hydrodynamic scaling studies of imploding spherical plasma liners, *Phys. Plasmas*, **18**, 072705, 2011.

[8] J. T. Cassibry, M. Stanic, S. C. Hsu, S. I. Abarzhi, F. D. Witherspoon, Tendency of spherically imploding plasma liners formed by merging plasma jets to evolve toward spherical symmetry, *Phys. Plasmas*, **19**, 052702, 2012.

[9] R. Samulyak, T. Lu, and P. Parks, A magnetohydromagnetic simulation of pellet ablation in electrostatic approximation, *Nuclear Fusion*, **47**, 103–118, 2007.

[10] H. Kim, R. Samulyak, L. Zhang, P. Parks, Influence of atomic processes on the implosion of plasma liners, *Phys. Plasmas*, **19**, 082711, 2012.

[11] Ya. B. Zel′dovich and Yu. P. Raizer, Physics of shock waves and high-temperature hydrodynamic phenomena, *Dover*, 2002.

[12] R. E. Siemon, I. R. Lindemuth, and K. F. Schoenberg, Why MTF is a low cost path to fusion, *Comments Plasma Physics Controlled Fusion*, **18**, 363386, 1999.

[13] Y. C. F. Thio, E. Panarella, C. E. Knupp R. C. Kirkpatrick, F. Wysocki, P. Parks, and G. Schmidt, Magnetized target fusion in a spheroidal geometry with standoff drivers, *in Current Trends in International Fusion Research II, edited by E. Panarella, National Research Council Canada, Ottawa, Canada*, 1999.

[14] P. B. Parks, On the efficacy of imploding plasma liners for magnetized fusion target compression, *Phys. Plasmas*, **15**, 062506, 2008.

[15] J. T. Cassibry, R. J. Cortez, S. C. Hsu, and F. D. Witherspoon, Estimates of confinement time and energy gain for plasma liner driven magnetoinertial fusion using an analytic self-similar converging shock model, *Phys. Plasmas*, **16**, 112707, 2009.

[16] S. C. Hsu, T. J. Awe, S. Brockington, A. Case, J. T. Cassibry, G. Kagan, S. J. Messer, M. Stanic, X. Tang, D. R. Welch, and F. D. Witherspoon, Spherically Imploding Plasma Liners as a Standoff Driver for Magnetoinertial Fusion, *IEEE Trans. Plasma Science*, **40**, 1287, 2012.

[17] H. Kim, L. Zhang, R. Samulyak, P. Parks, On the Structure of Plasma Liners for Plasma Jet Induced Magnetoinertial Fusion, *Phys. Plasmas*, **20**, 022704, 2013.

[18] L. Baylor and et al., Improved core fueling with high field pellet injection in the DIII-D tokamak, *Phys. Plasmas*, **7**, 18781885, 2000.

[19] L. Baylor and et al., Comparison of fueling efficiency from different fueling locations on DIII-D, *J. Nucl. Materials*, **313**, 530533, 2003.

[20] P. T. Lang and et al., High density operation in H mode discharges in inboard launch pellet refuelling, *Nuclear Fusion*, **40**, 245260, 2000.

[21] B Pgouri, Review: Pellet injection experiments and modelling, *Plasma Phys. and Controlled Fusion*, **49**, R87, 2007.

[22] S. C. Jardin and et al., A fast shutdown technique for large tokamaks, *Nucl. Fusion*, **40**, 923933, 2000.

[23] R. Ishizaki, P. Parks, N. Nakajima, M. Okamoto, Two-dimensional simulation of pellet ablation with atomic processes, *Phys. Plasmas*, **11**, 4064, 2004.

[24] P. Parks, T. Lu, and R. Samulyak, Charging and $E \times B$ rotation of ablation clouds surrounding refueling pellets in hot fusion plasmas, *Phys. Plasmas*, **16**, 060705, 2009.

[25] H. R. Strauss and W. Park, Pellet driven disruptions in tokamaks, *Phys. Plasmas*, **7**, 250257, 2000.

[26] R. Samtaney and et al., 3D Adaptive mesh refinement simulations of pellet injection in tokamaks, *Computer Physics Comm.*, **164**, 220228, 2004.

[27] P. Colella and et al., Chombo software package for AMR applications design document.

[28] P. Parks and et al., Radial displacement of pellet ablation material in tokamaks due to the grad-B effect, *Phys. Plasmas*, **7**, 19681975, 2000.

[29] P. Parks, R. J. Turnbull, Effect of transonic flow in the ablation cloud on the lifetime of a solid hydrogen pellet in a plasma, *Phys. Fluids*, **21**, 1735, 1978.

[30] P. Parks, Magnetic-field distirsion near an ablating hydrogen pellet, *Nuclear Fusion*, **20**, 311-320, 1980.

[31] P. Parks and M. Rosenbluth, Equilibrium pellet and liquid jet shape under high ablation pressures, *Phys. Plasmas*, **5**, 1380 1386, 1998.

[32] P. Parks and L. R. Baylor, Effects of parallel flows and toroidicity on cross field transport of pellet ablation matter in tokamak plasmas, *Phys. Rev. Letters*, **12**, 125002, 2005.

[33] P. Parks, Theory of pellet cloud oscillation striations, *Plasma Phys. Control. Fusion*, **38**, 571-591, 1996.

[34] A. K. MacAulay, Two dimensional time dependent simulation of ablation of hydrogen pellets in hot magnetized fusion plasmas, PhD thesis, Princeton University, 1993.

[35] A. K. MacAulay, Geometrical, kinetic and atomic physics effects in a two dimensional time dependent simulation of ablating fuel pellets, *Nuclear Fusion*, **34**, 4362, 1994.

[36] B. Fix, J. Glimm, X. Li, Y. Li, X. Liu, R. Samulyak, and Z. Xu, A TSTT integrated FronTier code and its applications in computational fluid physics, *Journl of Physics: Conf. Series*, **16**, 471-475, 2005.

[37] B. van Leer, Towards the ultimate conservative difference scheme: V. A second order sequel to Godunov's method, *J. Comput. Phys.*, **32**, 101-136, 1979.

[38] R. Samulyak, J. Du, J. Glimm, and Z. Xu, A numerical algorithm for MHD of free surface flows at low magnetic reynolds numbers, *J. Comput. Phys.*, **226**, 1532-1546, 2007.

[39] W. F. Noh, Errors for calculations of strong shocks using an artificial viscosity and an artificial heat flux, *J. Comput. Phys.*, **72**, 78-120, 1987.

[40] J. J. MacFarlane, I. E. Golovkin, and P. R. Woodruff, HELIOS-CR A 1-D radiation-magnetohydrodynamics code with inline atomic kinetics modeling, *J. Quant. Spectrosc. Radiat. Transf.*, **99**, 381, 2006.

[41] See https://wci.llnl.gov/codes/visit/.

[42] R. Menikoff and B. J. Plohr, The Riemann problem for fluid flow of real materials, *Rev. Mod. Phy.*, **61**, 75-128, 1989.

[43] F. S. Felber, P. B. Parks, R. Prater, and D. F. Vlasow, Effect of atomic processes on fuel pellet ablation in thermonuclear plasma, *Nucl. Fusion*, **19**, 1061, 1979.

[44] J. Du, B. Fix, J. Glimm, X. Jia, X. Li, Y. Li, and L. Wu, A simple package for front tracking, *J. Comput. Phys.*, **213**, 613-628, 2006.

[45] S. C. Hsu et al., Experimental characterization of railgun-driven supersonic plasma jets motivated by high energy density physics applications, *Phys. Plasmas*, **19**, 123514, 2012.

[46] J. S. Davis, S. C. Hsu, I. E. Golovkin, J. J. MacFarlane, and J. T. Cassibry, One-dimensional radiation-hydrodynamic simulations of imploding spherical plasma liners with detailed equation-of-state modeling, *Phys. Plasmas*, **19**, 102701, 2012.

[47] J. Santarius, Compression of a spherically symmetric deuterium-tritium plasma liner onto a magnetized deuterium-tritium target, *Phys. Plasmas*, **19**, 072705, 2012.

[48] E. Merritt, PLX is assessing single and merged plasma jet properties in support of plasma liner experiments, *54th Annual Meeting of the APS-DPP*, 2012.

[49] E. Merritt et al., Experimental characterization of the stagnation layer between two obliquely merging supersonic plasma jets, *Phys. Rev. Lett.*, **111**, 085003, 2013.

[50] E. Merritt et al., Experimental evidence for collisional shock formation via two obliquely merging supersonic plasma jets, *Phys. Plasma*, **21**, 055703, 2014.

[51] See http://www.prism-cs.com.

[52] H. R. Griem, Validity of local thermal equilibrium in plasma spectroscopy, *Phys. Rev.*, **131**, 1170-1176, 1963.

[53] See http://people.sc.fsu.edu/ jburkardt/f_src/sphere_cvt/sphere_cvt.html for further information about SCVT software.

[54] Q. Du, V. Faber, M. Gunzburger, Centroidal Voronoi Tessellations: Applications and Algorithms, *SIAM Review*, **41**, 637-676, 1999.

[55] J.D. Huba, NRL Plasma Formulary, 2011.

[56] Charles E. Knapp, An implicit smooth particle hydrodynamic code, *PhD thesis, Los Alamos national laboratory*, 2000.

[57] R. Courant, K.O. Friedrichs, Supersonic Flow and Shock Waves, *Springer*, 1991.

[58] AMES Research Staff, Report 1135, Equations, tables, and charts for compressible flow.

[59] P. Parks, W. D. Sessions, L. R. Baylor, Radial displacement of pellet ablation material in tokamaks due to the grad-B effect, *Phys. Plasmas*, **5**, 1968, 2000.

[60] ICRU Report 37, Stopping powers and ranges for protons and alpha particles ,*International Commission of Radiation Units and Measurement*, 1984.